# A cuttlefish ink nanoparticle-reinforced biopolymer hydrogel with robust adhesive and immunomodulatory features for treating oral ulcers in diabetes

Yajing Xiang [a,1], Zhuge Pan [b,1], Xiaoliang Qi [c,***], XinXin Ge [a], Junbo Xiang [d], Hangbin Xu [a], Erya Cai [a], Yulong Lan [d], Xiaojing Chen [d], Ying Li [d], Yizuo Shi [a], Jianliang Shen [c,d,**], Jinsong Liu [a,*]

[a] School & Hospital of Stomatology, Wenzhou Medical University, Wenzhou, Zhejiang, 325027, China
[b] Department of Otolaryngology, Affiliated Jinhua Hospital, Zhejiang University School of Medicine, Jinhua, Zhejiang, 321000, China
[c] National Engineering Research Center of Ophthalmology and Optometry, Eye Hospital, Wenzhou Medical University, Wenzhou, Zhejiang, 325027, China
[d] Zhejiang Engineering Research Center for Tissue Repair Materials, Wenzhou Institute, University of Chinese Academy of Sciences, Wenzhou, Zhejiang, 325001, China

## ARTICLE INFO

## ABSTRACT

Oral ulcers can be managed using a variety of biomaterials that deliver drugs or cytokines. However, many patients experience minimal benefits from certain medical treatments because of poor compliance, short retention times in the oral cavity, and inadequate drug efficacy. Herein, we present a novel hydrogel patch (SCE2) composed of a biopolymer matrix (featuring ultraviolet-triggered adhesion properties) loaded with cuttlefish ink nanoparticles (possessing pro-healing functions). Applying a straightforward local method initiates the formation of a hydrogel barrier that adheres to mucosal injuries under the influence of ultraviolet light. SCE2 then demonstrates exceptional capabilities for near-infrared photothermal sterilization and neutralization of reactive oxygen species. These properties contribute to the elimination of bacteria and the management of the oxidation process, thus accelerating the healing phase's progression from inflammation to proliferation. In studies involving diabetic rats with oral ulcers, the SCE2 adhesive patch significantly quickens recovery by altering the inflamed state of the injured area, facilitating rapid re-epithelialization, and fostering angiogenesis. In conclusion, this light-sensitive hydrogel patch offers a promising path to expedited wound healing, potentially transforming treatment strategies for clinical oral ulcers.

## 1. Introduction

Oral ulcers, also known as injuries to the oral mucosa, represent common and recurrent conditions in oral health, marked by the persistent destruction or impairment of the oral epithelial tissue [1]. Globally, over 25 % of individuals have suffered or are currently suffering from these ulcers [2,3]. Oral ulcers that are not treated or poorly managed can cause the loss of epithelial tissue, creating cavities or, in extreme situations, leading to tissue death. Such conditions make fundamental activities such as eating, swallowing, talking, and digesting difficult for individuals [4]. Furthermore, the absence of the natural protective barrier of the oral mucosa renders these wounds prone to bacterial infections, thereby diminishing the speed of ulcer healing [5, 6]. Although various treatments like oral ulcer patches (comprising chitosan and flavonoids), powders (containing vitamins), and ointments (such as recombinant human epidermal growth factor gel) are available to expedite the healing process, their effectiveness is limited [7–9]. The constraint arises from their short-lived adhesion to the mucosal surface

within the moist and dynamic environment of the oral cavity, typically enduring for less than 2 h. Therefore, the development of biomaterials with improved adhesive qualities is essential for accelerating the healing process of oral ulcers.

Creating hydrogel patches that possess adhesive properties is considered an effective strategy for addressing oral ulcers [10]. The methods of adhesion for these hydrogels are generally categorized into two types: chemical and physical, with the majority depending on a transition from a liquid state to a solid one to achieve adherence [11,12]. Physical adhesion often utilizes hydrogen bonds, yet strong adhesion is challenging to achieve and tends to fail in a moisture-rich oral environment [13,14]. Consequently, approaches focused on creating chemical connections with the tissue interface provide strong

attachment and support cellular movement at the location of adhesion [15,16]. Research has shown that a hydrogel comprising N-(2-amino-ethyl)-4-(4-(hydroxymethyl)-2-methoxy-5-nitrosophenoxy)butanamide (NB)-modified hyaluronic acid (HA-NB) and methacrylated gelatin (GelMA) displays several benefits [17,18]. These include potent adhesion to wet tissue, quick gelation, minimal swelling, and high biocompatibility, all crucial attributes for use in the moisture-laden environment of the oral cavity [19]. HA-NB and GelMA, the fundamental components of the hydrogel, reflect the extracellular matrix's (ECM) structure found in the oral mucosa, predominantly consisting of proteins and polysaccharides [18,20]. As a result, such an ECM-simulating adhesive hydrogel might serve as an ideal substance for accelerating the repair of injuries in the oral mucosa.
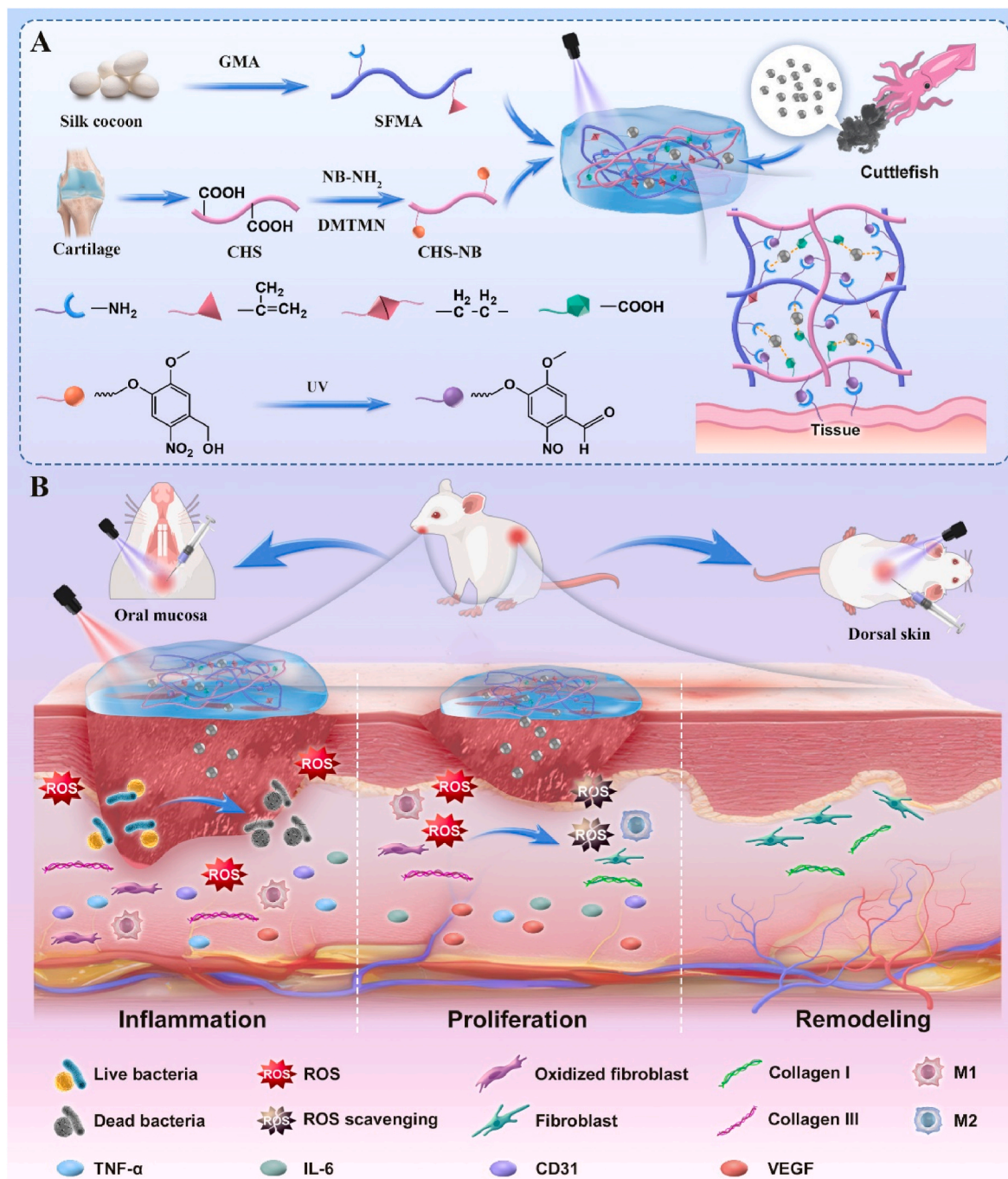


**Scheme 1.** Fabrication and usage of SCE2 hydrogel for accelerated healing in oral ulcers among bacteria-infected diabetic rats. (A) Synthesis process of the SCE2 hydrogel. (B) Mechanisms of SCE2 hydrogel in enhancing wound recovery.

After achieving adhesion properties, the precise coordination of biological activities within hydrogel dressings is essential for the effective healing of wounds caused by oral ulcers. Like skin wound healing, the recovery process of oral ulcers typically involves three consecutive yet interrelated stages: inflammation, cellular proliferation, and tissue restructuring [21,22]. For the repair of oral mucosal injuries, oral mucoadhesive hydrogels must independently adjust the wound's microenvironment. This adjustment involves tackling inflammation, bacterial invasions, and the activity of host cells, all while protecting the wound's surface within a saliva-rich environment over a prolonged period (ideally exceeding 12 h), which is considered optimal for addressing issues related to oral mucosal regeneration [23]. Lately, various bioactive substances have been integrated into hydrogels for skin wound healing, which speed up tissue repair through sterilization, reduce inflammation, and stimulate growth factor release, thus bypassing the need for drugs, cell-based treatments, or cytokines [24, 25]. However, these bioactive agents frequently lack enduring adhesion and stability in damp environments [2,26]. Moreover, the complexity of their structural configurations, functional modifications, and the requirement for external interventions complicate their use in clinical settings. Thus, there is an urgent demand for the creation of oral ulcer dressings that exhibit strong adhesion (encompassing both chemical and physical aspects) and potent healing (biological) properties [24].

In the current research, focused on enhancing the treatment of oral ulcers, we aim to create an ECM-like hydrogel dressing, designated SCE2, that combines a biopolymer matrix [consisting of methacrylate silk fibroin (SFMA) and nitrobenzyl-modified chondroitin sulfate (CHS-NB) with light-responsive gelling and adhesion properties] with cuttlefish ink nanoparticles (known for their healing benefits) [27–29]. As illustrated in Scheme 1, exposure to 365 nm light triggers the formation of a safeguarding hydrogel coating on the wound via the radical polymerization of SFMA's double bonds. Concurrently, the hydrogel demonstrates robust adherence to moist tissues as the o-nitrobenzene group in its precursor CHS-NB transforms into an aldehyde group under the same light conditions. This transformation enables quick, strong attachment to the tissue via imine bond interactions with the tissue's surface amino groups. Additionally, cuttlefish ink nanoparticles within the SCE2 hydrogel exhibit exceptional abilities for near-infrared photothermal sterilization and neutralization of reactive oxygen species. Such characteristics aid in the elimination of bacteria and the control of oxidative conditions, thus accelerating the wound's shift from an inflammatory stage to a proliferative phase. SCE2's unique three-dimensional network, composed of elements derived from natural sources, potentially acts as a supportive reservoir, offering both nutritional and mechanical assistance to cells. This environment fosters cell attachment, movement, growth, and eventual angiogenesis in the process of tissue reconstruction. The SCE2 hydrogel's capacity to enhance wound recovery was validated through experiments with a streptozotocin-induced diabetic rat model. In summary, the SCE2 hydrogel exhibits considerable promise for its clinical use in swiftly healing oral ulcers.

## 2. Materials and methods

### 2.1. Materials

Silkworm cocoons were obtained from the Sericulture Technology Extension Station (Chongqing, China). N-(2-aminoethyl)-4-[4-(hydroxymethyl)-2-methoxy-5-nitrophenoxy]butanamide (NB–NH$_2$) was obtained from Chaocheng Technology (Haining, Zhejiang). Aladdin (Shanghai, China) provided N-hydroxysuccinimide (NHS), chondroitin sulfate (sourced from sharks with purity >99 %, and M$_w$ = 340 kDa), 4-(4,6-dimethoxy-1,3,5-triazin-2-yl)-4-methyl morpholinium chloride, glycidyl methacrylate (GMA), sodium carbonate (Na$_2$CO$_3$), dimethyl sulfoxide, lithium bromide (LiBr), N-(3-dimethylaminopropyl)-N′-ethylcarbodiimide hydrochloride (EDC·HCl), glycidyl methacylate, and

lithium phenyl(2,4,6-trimethylbenzoyl)phosphinate (LAP). 2-Morpholinoethanesulfonic acid was provided by Macklin (Shanghai, China). Hydrogen peroxide (H$_2$O$_2$) was provided by Sigma (Shanghai, China). Innochem (Beijing, China) provided 1,1-diphenyl-2-picrylhydrazyl (DPPH) and calcein acetoxymethyl ester. Yeasen (Shanghai, China) was the provider of propidium iodide (PI) and streptozotocin (STZ). Beyotime (Nanjing, China) supplied 2,2′-azino-bis (3-ethylbenzothiazoline-6-sulfonic acid), Cell Counting Kit (CCK)-8, and 2′,7′-dichlorofluorescein diacetate. SYTO9 was provided by Thermo Fisher (Waltham, USA). Gibco (NY, USA) was responsible for supplying fetal bovine serum, penicillin-streptomycin, Dulbecco's modified Eagle's medium (DMEM), and phosphate buffer saline (PBS). Hopebiol (Qingdao, China) was responsible for supplying Tryptic Soy Broth, agar powder, and Luria-Bertani Broth. All additional reagents and solvents, unless noted otherwise, were used in their original state and were of analytical reagent grade.

### 2.2. Synthesis of cuttlefish ink nanoparticles

Nanoparticles derived from cuttlefish ink (CFI) were extracted using differential centrifugation from a fresh cuttlefish's ink sac. To begin, the mixture with CFI nanoparticles underwent centrifugation at 2100 rpm for a duration of 5 min, aiming to eliminate sizable precipitates. Following this, it was centrifuged once more at 12,000 rpm for 10 min to harvest the CFI nanoparticles. Finally, the CFI nanoparticles were thoroughly rinsed with double distilled water (DDW) and subsequently suspended in DDW for later use.

### 2.3. Synthesis of methacrylate silk fibroin (SFMA) and nitrobenzyl-modified chondroitin sulfate

Synthesis of SFMA: Silk fibroin was fabricated by initially cutting silkworm cocoons into broken strips, which were then boiled in 0.02 M Na$_2$CO$_3$ for 30 min to eliminate the sericin layer. Post-degumming, the acquired fibers underwent rinsing with DDW, followed by air-drying at 37 °C. These were then dissolved in a 9.3 M LiBr solution at 65 °C for a period of 4 h. Subsequently, the obtained silk fibroin solution was moved into a dialysis bag (MWCO, 3.5 kDa) for dialysis. This process, conducted against DDW for 48 h, included six changes of DDW, facilitating the removal of lithium bromide. After dialysis, the silk fibroin solution underwent centrifugation at 9000 rpm for 15 min at 4 °C, repeated twice. The final step involved acquiring silk fibroin through freeze-drying.

To synthesize SFMA, 10 g of freeze-dried silk fibroin was combined with 40 mL of PBS (pH = 8.5) and stirred for 3 h. Meanwhile, in another vessel, 2.93 g of GMA was merged into 100 mL of PBS solution (pH = 8.5) under constant agitation. Following this, the GMA mixture was slowly added to the silk fibroin blend, creating the reaction mixture. After allowing the reaction between GMA and silk fibroin at room temperature overnight, the mixture was subjected to dialysis using bags (molecular weight = 3.5 kDa) in DDW for a week. The dialyzed SFMA was then freeze-dried for subsequent use.

Synthesis of nitrobenzyl-modified chondroitin sulfate (CHS-NB): Dissolving 2 g of chondroitin sulfate in 100 mL of 2-morpholinoethanesulfonic acid solution (0.01 M, pH 5.17) initiated the process. After that, 60 mg (0.18 mmol) of NB-NH$_2$, previously dissolved in dimethyl sulfoxide, was incorporated into the mixture. In a separate step, 1.2 g (1.36 mmol) of 4-(4,6-dimethoxy-1,3,5-triazin-2-yl)-4-methyl morpholinium chloride, after being dissolved in DDW, was divided and introduced in three equal segments, each separated by a period of 0.5 h. The acquired mixture was then stirred in a dark environment at 35 °C for 3 h. Next, dialysis of the mixture against a 0.1 M sodium chloride solution took place over three days, leading to its subsequent freezing and lyophilization.

## 2.4. Preparation of SCE2 hydrogel

In this research, we developed hybrid hydrogels integrating SFMA, CHS-NB, and CFI nanoparticles (abbreviated as SCE). The process began with mixing 1 mL of a 10 % (w/v) SFMA solution containing 8 mg of LAP photoinitiator with 1 mL of a 2 % (w/v) CHS-NB solution, which included varying amounts of CFI nanoparticles. This mixture was then exposed to ultraviolet light for 1 min, triggering a free radical polymerization reaction due to the residual double bonds, resulting in the formation of a hydrogel. Four different SCE hydrogels were produced, each with distinct CFI nanoparticle concentrations of 0, 0.5, 1, and 2 mg/mL, labeled SCE0, SCE1, SCE2, and SCE3, respectively.

## 2.5. Characterization of physicochemical traits

### 2.5.1. Spectra of proton nuclear magnetic resonance ($^1H$ NMR)

Deuterium oxide served as the solvent for preparing samples intended for $^1H$ NMR analysis, which were examined using a Quantum-I 400 MHz instrument from China. The $^1H$ NMR spectra obtained were subsequently processed and analyzed with Mestrenova software.

### 2.5.2. Thermogravimetric analysis (TGA)

TGA was conducted using a TGA8000 PerkinElmer thermo-analyzer (USA). In an air environment, the samples underwent examination. The TGA curves were traced from 50 to 600 °C, applying a consistent heating rate of 20 °C per minute.

### 2.5.3. Fourier transform infrared (FTIR) spectra

The functional groups of the CFI nanoparticles and SCE hydrogels were assessed employing the Bruker Tensor II FTIR spectrometer from Germany. The scan range for these samples was adjusted to span from 4000 to 400 $cm^{-1}$.

### 2.5.4. Zeta potentials

The zeta potentials of the samples were determined using a Multisizer 4e Coulter Counter (USA).

### 2.5.5. Ultraviolet–visible–near-infrared (UV–VIS–NIR) test

UV–VIS–NIR spectrum was carried out using a Cary5000 spectrophotometer (Agilent, USA) at ambient temperature.

### 2.5.6. Dynamic light scattering (DLS) measurements

DLS was performed using a Zetasizer nano series instrument (Malvern, UK), which features a He–Ne laser (633 nm, 4.0 mW). For calculating the average diameters of particles, analyses of the autocorrelation functions were performed using the cumulants approach. A minimum of three assessments were conducted for each specimen at 25 °C, following a 3-min stabilization period before starting the measurements.

### 2.5.7. Scanning electron microscope (SEM)

The surface of the CFI nanoparticles and freeze-dried hydrogels was sprayed with platinum using an EM ACE600 from Leica (Germany). Subsequently, the sample surface morphology was observed using a field emission SEM from Hitachi (SU8010, Japan), which operated at an acceleration voltage of 5 kV. The pore diameter of the SCE hydrogels was quantified using ImageJ software.

### 2.5.8. Transmission electron microscope (TEM)

For TEM analysis, samples were examined with a Jeol JEM-1230 TEM from Japan, which was set to function at 100 kV.

### 2.5.9. Swelling

Initially, SCE hydrogel samples, each with a predetermined weight, were placed in PBS at 25 °C to reach a state of equilibrium. Throughout the swelling process, the SCE hydrogels were periodically removed at set intervals. Moisture on the hydrogel surfaces was removed by gently pressing with damp filter papers. Subsequently, the wet weight of each SCE hydrogel was precisely determined using a BSA224S-CW electronic scale (Sartorius, Germany). To calculate the swelling ratio, the formula $(M_1 – M_2)/M_2$ was used, where $M_1$ is the weight of the hydrogel in its swollen state, and $M_2$ is its weight when dry [30].

### 2.5.10. Water retention

The freeze-dried SCE hydrogels were immersed in deionized water until a state of equilibrium was attained. The weights of these fully saturated SCE hydrogels were documented ($W_f$). The SCE hydrogels were then positioned in an oven set at 37 °C. At specified intervals, the weights of the SCE specimens were registered ($W_t$), and the water retention percentage was computed employing the following equation: Water Retention (%) = $W_t/W_f \times 100$ % [31].

### 2.5.11. Hydrogel adhesion performance

The adhesive strength of SCE hydrogels to biological tissues was assessed using fresh pig skin in accordance with the ASTM standards (F2255–05 and F2258-05). Before the tests, slices of pork skin were prepared and treated overnight with an EDC/NHS solution. A 200 μL quantity of the hydrogel precursor was applied to a 1 cm × 1 cm section of two pig skin pieces and then cross-linked under ultraviolet light for 1 min. The resulting SCE hydrogels were subjected to tensile tests to the point of failure. These tests were conducted on an Instron 5944 machine, which applied a stretching speed of 8 mm/min.

### 2.5.12. Rheological properties

The rheological characteristics of the synthesized SCE hydrogels were investigated at 25 °C employing a DHR-2 rheometer (TA, USA) in a stress-controlled mode. In the experiments, to prepare a sample compatible with the instrument's shear disc, the SCE hydrogel precursor was dispensed into a plastic mold with dimensions of 25 mm in diameter and 1 mm in height. Strain sweep tests ranged from 0.1 % to 2000 % oscillatory strains at a constant frequency (1 Hz) to explore the linear viscoelastic regions. Based on the strain sweep outcomes, the oscillation strain was set at 1 %. Sweep analyses were conducted to examine the relationship between modulus and frequency (0.01–100 Hz). The SCE hydrogels' capacity for self-repair was evaluated through dynamic step-strain analyses, alternating the oscillatory strain between 1000 % and 1 % for every cycle. Investigations into the shear-thinning properties of the SCE samples were carried out employing steady-rate sweep analyses, where shear rates ranged between 0.1 and 100 1/s.

### 2.5.13. Investigating photothermal characteristics

Photothermal properties of CFI nanoparticles and SCE hydrogels underwent assessment through an experiment utilizing NIR laser light. To investigate the photothermal impact under 808 nm laser light, samples at different concentrations (2, 1.0, and 0.5 mg/mL) of CFI nanoparticles and SCE hydrogels were organized into 1.5 mL tubes. Monitoring and recording of temperature alterations in these materials were executed continuously using an E4 FLIR infrared camera (USA). Subsequent evaluations were made on how varying NIR laser powers (2.0, 1.0, and 0.5 $W/cm^2$) affected the photothermal efficiency of the materials. Additionally, the resilience of CFI nanoparticles and hydrogels under photothermal conditions was examined across four laser on-and-off cycles. The photothermal conversion efficiency (η) of the created samples was determined by subjecting them to 808 nm NIR light at 1 $W/cm^2$ for 5 min and then turning off the laser. Temperature variations in the materials were closely tracked with a FLIR thermal imaging camera.

### 2.5.14. Reactive oxygen species (ROS) scavenging capability

CFI nanoparticles and SCE2 hydrogel's antioxidant abilities were assessed by conducting a DPPH radical scavenging assay, which measured their capacity to neutralize free radicals. A new solution of DPPH in ethanol (0.1 mM) was mixed for the test. Subsequently,

specimens were immersed in the DPPH solution and kept in the dark at 37 °C for a set duration. Then, the reactive mixture's absorbance was gauged at a wavelength of 517 nm. The DPPH scavenging ability percentage was determined with the equation: Inhibition (%) = $(1 - A_a/A_b)$ × 100 %. In this formula, $A_b$ represents the initial absorbance of the DPPH solution, while $A_a$ denotes the DPPH's absorbance after being mixed with the samples under test for a set duration.

Besides, the overall antioxidant capacity of the CFI nanoparticles and SCE2 hydrogel underwent evaluation through the 2,2'-azino-bis (3-ethylbenzothiazoline-6-sulfonic acid) (ABTS) assay. In a summarized procedure, hydrogels weighing 100 mg, containing varying concentrations of nanoparticles, were submerged in 1.0 mL of culture medium for 30 min. Adhering to the instructions supplied by the kit's producer, the extracts from these hydrogels were subjected to a total antioxidant capacity assay. The subsequent step involved measuring and comparing the solution absorbance at 734 nm.

Furthermore, the scavenging efficiency of the CFI nanoparticles and SCE2 hydrogel for superoxide radicals ($O_2^{\bullet-}$) was determined by the inhibition rate of nitro blue tetrazolium (NBT). A reaction mixture in PBS solution was prepared, containing NBT (336 μM), nicotinamide adenine dinucleotide (936 μM), phenazine methosulfate (120 μM), and the prepared materials. After removing the tested samples, the mixture was maintained at 37 °C for 6 min. Next, the absorbance of the specimens at 560 nm was documented. The scavenging capacity for $O_2^{\bullet-}$ in each sample was calculated with the equation: Inhibition (%) = $(1 - A_t/A_c)$ × 100 %. Here, $A_c$ refers to the absorbance in the blank control group, while $A_t$ indicates the absorbance in samples containing CFI nanoparticles or SCE2 hydrogel.

### 2.6. In vitro cell assays

#### 2.6.1. CCK-8 experiments

The cytotoxicity of the SCE hydrogels was assessed via the CCK-8 assay. Initially, all samples were immersed in cell culture media for 24 h to extract the SCE leachate. Then, RAW 264.7 and RS1 cells were planted in 96-well plates at a density of $5 \times 10^3$ cells per well, utilizing DMEM enriched with 10 % fetal bovine serum. Following a 24-h period, the medium for cell culture was discarded. Subsequently, cells underwent exposure to leachate from the hydrogel, undergoing incubation periods of 1, 3, and 5 days. At specific intervals, the medium was replenished with fresh media containing 10 % CCK-8. After incubating the solution in darkness for 2 h, its absorbance was measured at 450 nm with a Thermo Fisher spectrophotometer (1530, USA). Cell viability was calculated using the formula Cell Viability (%) = $A_t/A_i$ × 100 %, where $A_i$ represents the absorbance of the control, and $A_t$ is the absorbance of the treatment group. This process involved five sets of parallel experiments, each conducted in duplicate.

Besides, cell viability was evaluated through live/dead cell staining to observe the survival state of the cells. Specifically, RAW 264.7, RS1, and HGF cells were initially plated at a density of $5 \times 10^4$ cells per well in confocal dishes and incubated for 12 h. These dishes subsequently received treatments with hydrogel leaching solutions. Post a culture period of three days, staining of both live and dead cells was performed utilizing a calcein acetoxymethyl ester (calcein-AM)/PI staining kit. Observations of the cellular fluorescence were made with a Leica confocal microscope.

#### 2.6.2. Antioxidant tests

The protective effects of CFI nanoparticles and SCE hydrogels against intracellular oxidative stress were investigated by evaluating cell survival following exposure to $H_2O_2$ and treatments with CFI nanoparticles or hydrogels. RS1 cells and RAW 264.7 macrophages were incubated in 96-well plates at a concentration of $1 \times 10^4$ cells per well and were permitted to proliferate overnight. Cells cultured in media supplemented with $H_2O_2$ served as the positive control. Subsequently, cultures were treated with variously processed $H_2O_2$, followed by a 6-h

incubation. Cell viability was then determined using the CCK-8 assay.

To further investigate the intracellular antioxidant capabilities of the hydrogels, a green fluorescent probe for ROS, 2′,7′-dichlorofluorescein diacetate (DCFH-DA), was employed to investigate intracellular ROS levels. HGF, RAW 264.7, and RS1 cells were cultured in confocal dishes and allowed to develop overnight. Following the removal of the cell culture medium, adherent cells were treated with the same volume of $H_2O_2$ or hydrogel extract for 6 h. The fluorescent probe DCFH-DA was then introduced. Afterward, fluorescence microscopy was used for cell imaging. For quantitative assessments, cells in 6-well plates underwent the same treatment previously outlined, aimed at detecting intracellular ROS. Following a 30-min DCFH-DA exposure period, these cells underwent trypsinization and were washed three times with PBS. The fluorescence intensity in the cells was later quantified through flow cytometry.

#### 2.6.3. Cell migration

RS1 cells were planted at a concentration of $3 \times 10^5$ cells per well. When achieving 90 % confluence, an artificial gap was generated among the cells by creating a linear scratch with a 10 μL pipette tip. Subsequently, cells that had detached were eliminated by washing thrice with pre-warmed PBS. Following this, RS1 cells were transferred to a fresh medium and treated with the same volume of either $H_2O_2$ or hydrogel extract. Observations of the cells were made under a microscope after incubation periods of 0, 12, and 24 h.

#### 2.6.4. Angiogenesis

Angiogenesis tests were performed to assess the cell's capacity to promote the formation of new blood vessels in conditions of oxidative stress. Usually, 50 μL of Matrigel was spread uniformly over a 96-well plate and solidified after incubating for 1 h. After this, human umbilical vein endothelial cells (HUVECs) were planted on the Matrigel with a density of $2 \times 10^4$ cells per well. Once adherence was achieved, either hydrogel extract or $H_2O_2$ was introduced. Afterward, the cells underwent an 8-h cultivation period. In the final step, they were stained for 20 min using a calcein-AM staining kit and then observed through a microscope.

#### 2.6.5. Transcriptome sequencing

RAW 264.7 macrophages were processed to extract total RNA utilizing Invitrogen Trizol reagent (California, USA). A Thermo Scientific spectrophotometer (NanoDrop 2000, USA) was employed to ascertain RNA's purity and concentration. Additionally, the RNA's integrity was verified via the Santa Clara Bioanalyzer (Agilent 2100, USA). Subsequently, RNA-seq library construction was performed using the VAHTS Universal V6 RNA-seq Library Prep Kit.

### 2.7. In vitro blood compatibility assay

The blood compatibility of SCE hydrogels was evaluated through a hemolytic assay. First, fresh whole blood was washed thrice with PBS at 3000 rpm for 5 min each. Blood that had been washed and resuspended to a volume of 0.6 mL received treatment with 60 mg of hydrogel placed in a 1.5 mL centrifuge tube for 2 h. For control sets, 60 mg of DDW and 60 mg of PBS were added to separate 0.6 mL blood samples, serving as negative and positive controls, respectively. Following treatment, each sample was subjected to centrifugation (3000 rpm for 4 min). Subsequently, the absorbance of the resultant solutions was determined at 545 nm utilizing a spectrophotometer.

### 2.8. In vitro antibacterial assays

#### 2.8.1. Bacterial preparation

The antibacterial activity of the SCE hydrogels was assessed employing methicillin-resistant *Staphylococcus aureus* (MRSA, ATCC 43310) and multidrug-resistant *Pseudomonas aeruginosa* (MRPA, ATCC

27853). The bacterial solution was first revived and cultured at 37 °C for 24 h. Subsequently, 10 mL of growth medium was combined with 100 μL of stock bacteria solution (either MRSA or MRPA, $5 \times 10^9$ CFU/mL). The mixture was then incubated overnight at 37 °C in a shaking incubator at 200 rotations per minute. Following this, the bacteria were diluted at a ratio of 1:1000 (v/v) for subsequent applications.

### 2.8.2. Studying photothermal antibacterial performance

100 mg of the samples (hydrogels or PBS) were mixed into 1 mL of the bacterial solution. After incubation and different treatments, 20 μL of this bacterial solution was uniformly spread onto agar plates. The plates were then incubated overnight to allow for bacterial colony formation. The colonies were subsequently counted and photographed for analysis.

### 2.8.3. Bacterial morphology observation

Morphological changes in bacteria after antibacterial assays were monitored using SEM and TEM imaging methods. In the SEM protocol, bacterial cultures (MRSA and MRPA) were collected, washed three times with PBS, and fixed in 2.5 % glutaraldehyde at 4 °C overnight. A dehydration sequence using increasing concentrations of ethanol was conducted prior to SEM examination. For TEM analysis, bacteria were first fixed in 2.5 % glutaraldehyde at 4 °C, followed by post-fixation with 1 % osmium tetroxide. Subsequently, the specimens were washed three times in PBS for 15 min each. Dehydration followed, using a series of ethanol treatments for 15 min at each concentration step. The prepared samples were then analyzed and imaged using TEM.

### 2.8.4. Bacterial live/dead staining

Additionally, the antibacterial properties of SCE hydrogels were examined through a bacterial live/dead staining assay. Post various treatments, the bacterial cells were co-stained with SYTO9 and PI for a duration of 20 min in the dark, followed by three washes with PBS. Following the manufacturer's instructions, all bacteria stained with SYTO9 presented green fluorescence, while those stained by PI, indicating dead bacteria, exhibited red fluorescence. The concluding step was to capture fluorescence images using a confocal microscope (Nikon, Japan).

### 2.9. Wound healing in vivo

### 2.9.1. Constructing the type 1 diabetic rat model

The animal study adhered to the policies and norms set by the Wenzhou Medical University Animal Experiment Center (authorization number Wydw7019-0134).

Male Sprague-Dawley rats, procured from Beijing Laboratory Animal Technology Co., Ltd (Vital River, China), were used. For the development of the type 1 diabetic wound model, male Sprague-Dawley rats received a 1 % STZ intraperitoneal injection after fasting for 12 h, thereby creating a model of diabetes in rats. One week after injection, blood glucose levels were randomly monitored by sampling blood from the tail vein. Rats exhibiting blood glucose levels exceeding 16.7 mM were considered successfully modeled for type 1 diabetes.

### 2.9.2. Constructing MRSA-infected back skin wounds

Prior to initiating the SCE hydrogel therapy, diabetic rodents underwent a fasting period of 4 h. After administering anesthesia, we shaved the rodents' backs and created full-thickness incisions along both sides of the spinal midline. Subsequently, full-thickness cutaneous lesions (8 mm in diameter) on the rodents received a 10 μL application of MRSA solution (concentration: $1 \times 10^7$ CFU/mL) to develop an infection in the wound model. We categorized the infected skin wounds into five distinct groups: one receiving only PBS (baseline group), another with 3 M Tegaderm film (positive control), one with SCE0 hydrogel, another with SCE2 hydrogel, and the last group received SCE2 hydrogel along with laser exposure (1.0 W/cm², duration: 3 min). We applied 100 mg of

the designated substances to each group. Measurements of the wound sizes were recorded on days 0, 3, 7, and 14.

### 2.9.3. Constructing MRSA-infected oral ulcer wounds

In order to establish the oral mucositis model in rats, we employed a modified version of the conventional technique. Once the diabetic rats were under anesthesia, we dried the mandibular mucosa of the Sprague-Dawley rats with sterile cotton. Subsequently, a square piece of filter paper (3 mm by 3 mm) was soaked in 50 % glacial acetic acid for 5 s and then quickly placed on the gingival mucosa. The filter paper remained on the mucosa for 30 s before removal, and the area was then cleansed employing a sterilized cotton ball dampened in PBS to eliminate any remaining acetic acid. The filter paper was then soaked in MRSA solution (concentration: $1 \times 10^7$ CFU/mL) for another 5 s. The ulcers generated were divided into five categories: one baseline group treated with PBS, a positive control group receiving dexamethasone membrane therapy, one set administered SCE0 hydrogel, another provided with SCE2 hydrogel, and the last group treated with SCE2 hydrogel before undergoing laser therapy (1.0 W/cm² for 3 min). Daily photographs were taken, and notes on the ulcers were documented.

### 2.9.4. Hemostatic assay

Initially, the hemostatic capabilities of the developed SCE2 hydrogel were assessed using a rat tail hemostasis model. The procedure involved cutting the rat's tail at the lower third with surgical scissors. After a 15-s interval, different materials (each weighing 200 mg) were applied to the tail wounds. The treatment procedure was captured in photographs, and the volume of blood loss was meticulously recorded.

To further explore the SCE2 hydrogel dressing's hemostatic effectiveness, a liver hemorrhage model was established. The rat's abdominal cavity was carefully opened through surgery, revealing the liver. We used absorbent paper to meticulously soak up any fluid seeping out. Next, a scalpel was employed to create an 8 mm in length and 1.5 mm in depth incision on the surface of the liver. Following this, we applied 200 mg of various substances to the damaged area on the rat's liver. This procedure was documented with photographs.

### 2.9.5. Photothermal performance

Diabetic rats were randomly assigned into three equal sets, each comprising three rats: SCE2, SCE0, and PBS. For the groups involving SCE0 and SCE2 hydrogels, the wound areas received NIR light treatment (808 nm, 1 W/cm², for 3 min). Thermal imagery of the areas was captured using infrared camera technology.

### 2.9.6. Biosafety evaluation

Following the in vivo studies on the healing of wounds infected with bacteria, blood specimens were collected from the rats to conduct biochemical analyses and routine blood examinations. Concurrently, key organs (heart, liver, spleen, kidney, and lung) of the type 1 diabetic rats were extracted and subjected to hematoxylin-eosin (H&E) staining for histological assessment.

### 2.9.7. Histological analysis

At the conclusion of the experiment, tissues from the dorsal skin and oral mucosa were harvested for histological analysis. A Leica microtome (Germany) facilitated the slicing of tissues into sections 40 μm thick. These samples were then fixed in 4 % paraformaldehyde for a full day and embedded in paraffin. Subsequently, the derived tissue sections underwent staining with H&E, as well as Masson, myeloperoxidase (MPO), tumor necrosis factor-alpha (TNF-α), CD86 (M1 macrophage marker), vascular endothelial growth factor (VEGF), CD206 (M2 macrophage marker) and platelet endothelial cell adhesion molecule-1 (CD31).

## 2.10. Statistical analysis

Analysis of the data was conducted through one-way ANOVA or the Student's t-test, with a P value of 0.05 or lower deemed statistically significant. The graphical representations displayed statistical outcomes as the average ± standard deviation. Within the graph legends, "NS" denotes a result that is not statistically significant (P greater than 0.05), while "*", "**", and "***" signify P values less than 0.05, 0.01, and 0.001, respectively.

## 3. Results and discussion

### 3.1. Preparation and characterization of CFI nanoparticles

The morphologies of the CFI nanoparticles, as seen under SEM and TEM, are depicted in Fig. 1A and B, respectively. We observed that the CFI displayed a uniform nanosphere shape devoid of discernible clumps. Complementing these findings, DLS analysis (Fig. S1, Supporting Information) suggested that the CFI had an average diameter of 177.4 ± 0.52 nm. Additionally, measurements indicated the CFI's zeta potential was −23.1 mV. This characteristic is presumably associated with the polyphenolic moieties present on the CFI surface, as detailed in Fig. S2 in the Supporting Information [32].

We undertook a systematic evaluation of CFI's near-infrared photothermal properties. We exposed various CFI concentrations to NIR radiation (808 nm, 1 W/cm$^2$) and monitored the process. Thermal imaging of CFI during irradiation was acquired using a FLIR infrared camera (as shown in Fig. 1C). As expected, CFI exhibited a greater temperature increase compared to PBS. Fig. 1D shows that the temperatures at CFI nanoparticle concentrations of 2, 1, and 0.5 mg/mL reached 81.6, 72.9, and 58.5 °C, respectively, after 10 min of exposure to the laser. The efficiency of CFI's photothermal conversion was also influenced by the power density of irradiation (Fig. S3, Supporting Information). The consistent temperature pattern of CFI across four heating and cooling cycles, depicted in Fig. 1E, indicated its reliable photothermal stability. Additionally, CFI's photothermal conversion rate was calculated to be 45.7 % (Figs. S4–S6, Supporting Information). These characteristics (high photothermal conversion efficiency and superior photothermal stability) make CFI nanoparticles an excellent candidate for photothermal antibacterial applications [33].

In light of the harmful effects of excessive ROS in diabetic wounds, materials capable of scavenging ROS have attracted significant interest. Considering the abundance of phenolic hydroxyl moieties on the CFI surface, we postulated that CFI might exhibit outstanding capabilities in scavenging free radicals. In this study, the ROS scavenging performance of CFI was evaluated through superoxide anion radical ($O_2^{\bullet-}$), ABTS, and DPPH assays (Fig. 1F–H). As predicted, CFI (1 mg/mL) achieved a clearance rate exceeding 70 % for various free radicals.

Following this, we examined CFI's cytoprotective capacity against oxidative stress induced by $H_2O_2$. After treating RAW 264.7 and RS1 cells with $H_2O_2$ and CFI, we assessed the intracellular antioxidant features by measuring cell viability. For example, after a 6-h exposure to 670 μM $H_2O_2$, the cell viability fell to 33.4 % for RAW 264.7 macrophages and to 40.5 % for RS1 cells. However, the cell survival rate was >65 % for CFI nanoparticles greater than 1 mg/mL (Fig. 1I and J). Moreover, the flow cytometry results, depicted in Fig. 1K and L, further confirmed that CFI protected RAW 264.7 macrophages and RS1 cells from oxidative damage, showing similar results. These findings demonstrate that CFI displays outstanding photothermal and ROS scavenging capabilities at concentrations of 1 and 2 mg/mL. Considering the cost-effectiveness of raw materials, we incorporated 1 mg/mL of the CFI system into the hydrogel for use as the primary subject in subsequent experiments.

### 3.2. Characterization of SCE2 hydrogel

Exploration of functional group transformations pre and post hydrogel fabrication utilized $^1$H NMR and FTIR techniques. Initially, notable variations in the $^1$H NMR spectra of SFMA were evident when contrasted with SF. In particular, the emergence of distinct signals at 5.60 ppm and 6.04 ppm, linked to the carbon-carbon double bond [34], was observed in the SFMA's $^1$H NMR data (Fig. 2A), indicating successful SFMA synthesis. Furthermore, Fig. 2B presents the $^1$H NMR spectrum for CHS-NB. Assigned peaks at 7.24 ppm and 7.76 ppm corresponded to the NB benzene ring, confirming the effective grafting of the NB group onto CHS [18,35]. Concurrently, SFMA's unique absorption bands at 1644 cm$^{-1}$ and 1518 cm$^{-1}$, representing the –CH$_2$=CH$_2$–, along with CHS-NB (–NB flexural vibration at 1564 cm$^{-1}$ and 1375 cm$^{-1}$) and CFI (–OH vibration at 3290 cm$^{-1}$), were detected in the FTIR spectrum of the CFI-integrated matrix, underscoring the successful creation of the SCE hydrogel (Fig. S7, Supporting Information).

Subsequently, a TGA test was conducted to investigate the thermal stability of the synthesized materials. Fig. 2C shows that the prepared samples underwent three distinct phases of decomposition. Initially, all samples demonstrated a gradual weight reduction up to 250 °C, mainly due to the evaporation of loosely bound water within the tested materials. During the second phase (between 250 and 400 °C), the hydrogel's mass diminished owing to the degradation of glycosidic links in the polysaccharide structure. In the final stage (beyond 400 °C), the decomposition of the SCE hydrogel began, leading to char formation due to the breakdown of the polymer chains. Furthermore, the total weight loss of the SCE0 and SCE2 hydrogels at 600 °C was 66.10 % and 64.41 %, respectively. TGA showed that SCE0 and SCE2 hydrogels exhibit comparable weight loss trajectories in an air environment, a finding consistent with their similar chemical makeup. Such results indicate the SCE hydrogel's superior thermal stability.

Following this, we utilized SEM to evaluate the surface texture and microscopic pore structure of the SCE specimens. As displayed in Fig. 2D and E, the porous mesh architecture of both SCE0 and SCE2 hydrogels provides an optimal environment for the absorption of exudates and cell growth. Further inspection through high-resolution SEM imagery indicated that the inner surface of SCE0 was comparatively smooth, whereas SCE2 exhibited a rougher texture, a result of integrating CFI nanoparticles. In addition, the mean pore size in SCE0 measured 26.82 μm while incorporating CFI into SCE2 resulted in a reduced average pore size of 20.14 μm (Figs. S8 and S9, Supporting Information).

Then, we assessed the hydrogel dressings for their ability to swell and deswell. As depicted in Fig. 2F, the swelling trajectories of SCE0 and SCE2 hydrogels revealed a comparable water uptake trend, marked by a consistent rise and eventual leveling off beyond 200 min. Upon reaching equilibrium, the SCE0 demonstrated a greater water absorption ratio (26.92) compared to SCE2 (21.86), suggesting that the hydrogels' crosslinking improved upon incorporating CFI [36]. In the water retention assessment, SCE2 demonstrated slightly superior water retention compared to SCE0 (Fig. 2G). These results suggest that the fabricated SCE2 hydrogel exhibits outstanding capabilities in absorbing and retaining water, enabling rapid absorption of wound exudate and preservation of a suitably moist environment conducive to wound healing [37].

### 3.3. Evaluating the antioxidant capacity of SCE2 hydrogel

An overabundance of ROS at wound locations may impede the process of healing. Therefore, herein, we integrated CFI into a SFMA/CHS-NB matrix and assessed the ability of the prepared nano-doping SFMA/CHS-NB system to neutralize free radicals, specifically $O_2^{\bullet-}$, ABTS, and DPPH. To begin, we focused on the superoxide anion radical, a prevalent type of ROS, and used an $O_2^{\bullet-}$ producing system, NADH-PMS-NBT, to test the hydrogels' neutralizing efficacy. The SCE2 hydrogel outperformed the SCE0 hydrogel, showing scavenging rates of 40.6 % and 13.5 %,
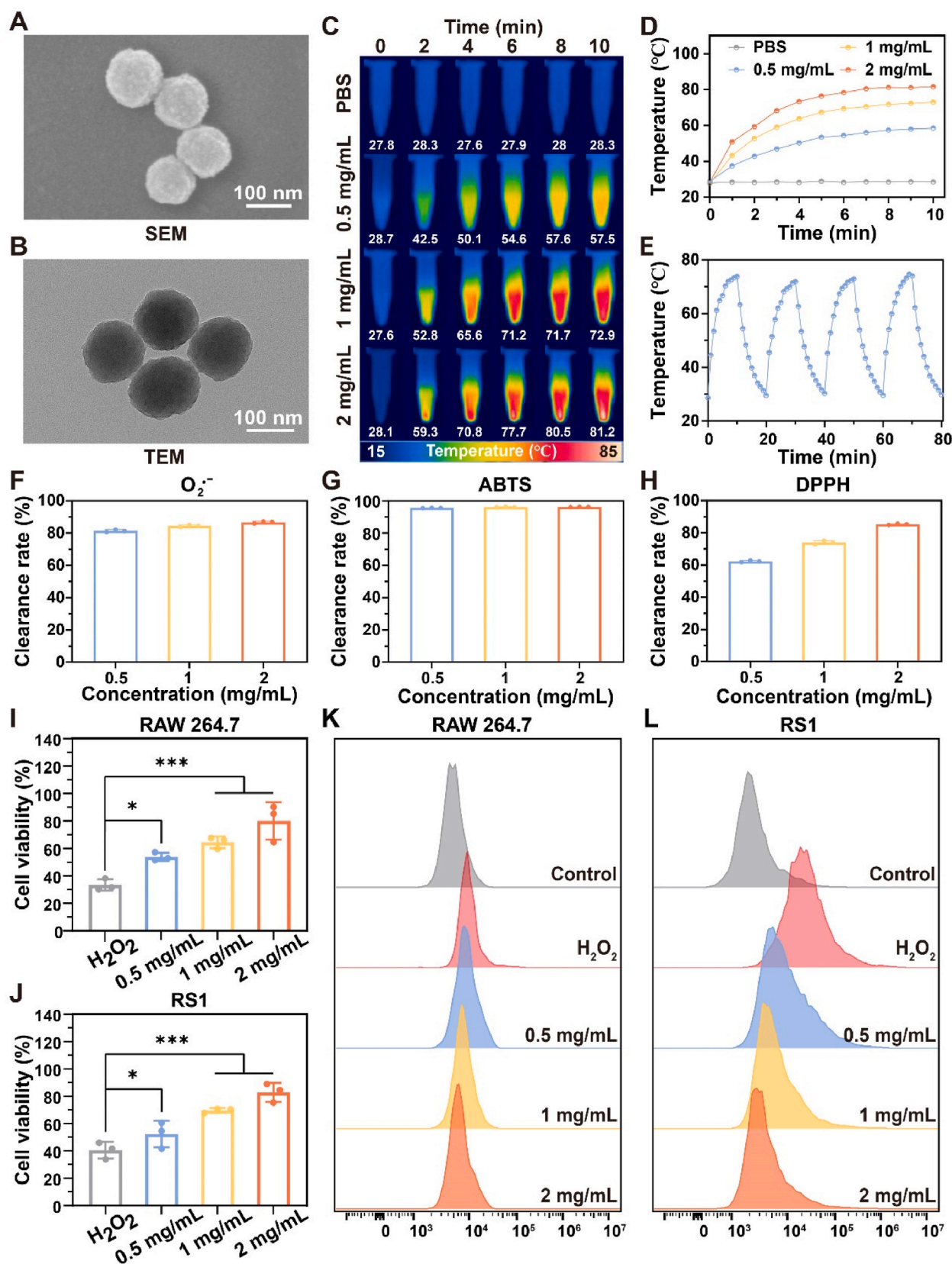
**Fig. 1.** Characterization of CFI nanoparticles. (A) SEM image of CFI. (B) TEM image of CFI. (C) Thermographs of different CFI concentrations over time. (D) Temperature increase profiles of CFI nanoparticles. (E) Photothermal cycling curve of 1 mg/mL CFI. (F–H) The effectiveness of CFI nanoparticles in neutralizing $O_2^{\bullet-}$ (F), ABTS (G), and DPPH radicals (H). (I and J) Evaluation of cell survival in RAW 264.7 (I) and RS1 (J) cells exposed to different concentrations of CFI nanoparticles in a solution with 670 μM $H_2O_2$, using the CCK-8 assay. (K and L) Flow cytometric assessment of RAW 264.7 macrophages (K) and RS1 cells (L). Error bars indicate the average ± standard deviation (n = 3). Levels of significance are denoted as *** for P < 0.001 and * for P < 0.05.
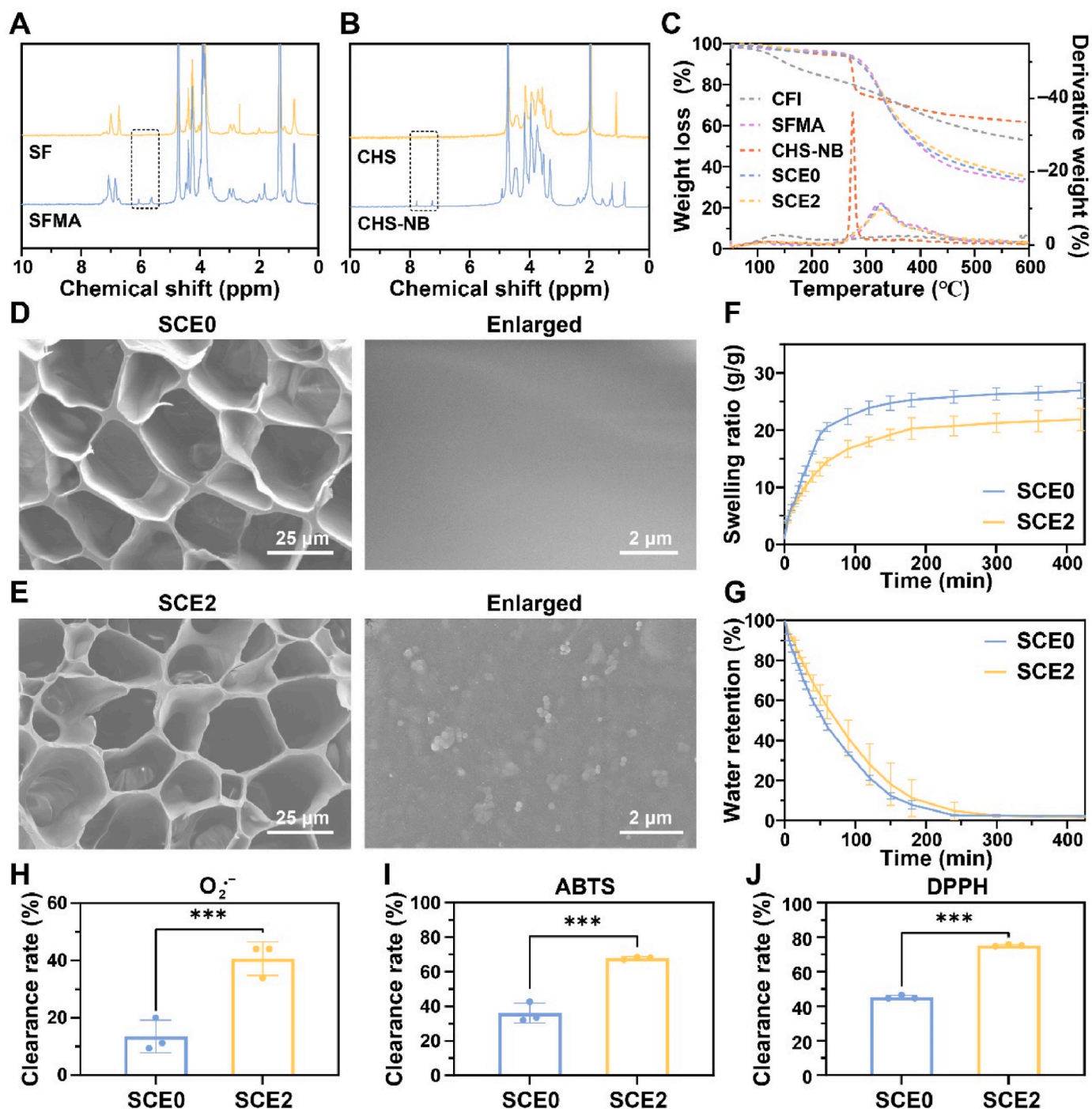
**Fig. 2.** Analyzing the physiochemical characteristics of SCE2 hydrogel. (A and B) Displaying $^1$H NMR spectra for SFMA (A) and CHS-NB (B). (C) TGA profiles of CFI and SCE hydrogels. (D and E) Diverse magnifications of SEM images featuring SCE0 (D) and SCE2 (E). (F and G) Performance in swelling (F) and deswelling (G) of SCE hydrogels. (H–J) Examining the radical scavenging abilities of SCE2 hydrogel against $O_2^{\bullet-}$ (H), ABTS (I), and DPPH (J). Error bars indicate the average $\pm$ standard deviation (n = 3). Significance levels: *** for P < 0.001.

respectively, as depicted in Fig. 2H. Further assessments of the hydrogels' antioxidant capabilities were conducted using ABTS (Fig. 2I), where the results aligned with those from the $O_2^{\bullet-}$ trials. Additionally, the SCE hydrogels underwent a 30-min incubation with DPPH. As expected, the CFI-enhanced SCE2 hydrogel exhibited more robust scavenging abilities than SCE0, as illustrated in Fig. 2J, confirming its superior antioxidant activity. The impressive radical neutralizing efficiency of SCE2 hydrogel suggests its potential as an antioxidant, which could be beneficial in promoting wound healing.

### 3.4. Assessment of SCE2 hydrogel's mechanical properties

Oral mucosa, being a moist and dynamic tissue, necessitates the creation of patches capable of forming stable, strong adhesion for treating oral ulcers. Essential features of mucosal hydrogel dressings, such as mechanical robustness and malleability, enable them to adapt to constantly varying and intricate wound environments. To assess the attachment of SCE hydrogels to tissues, macroscopic tests measuring adhesion were conducted on pig skin. The adhesive capabilities of these hydrogels were measured through lap-shear (Fig. 3A and B) and tension
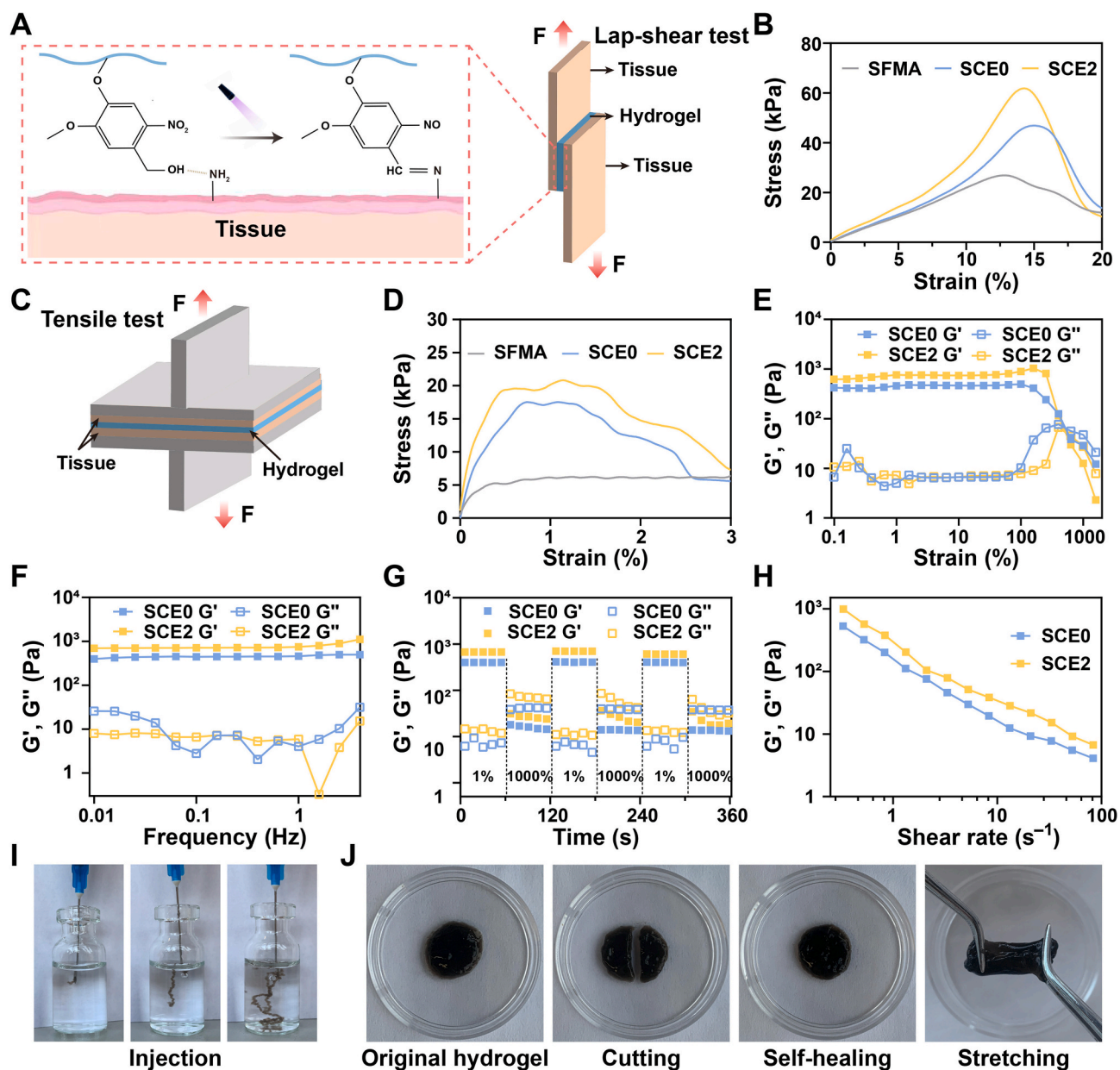
**Fig. 3.** Evaluating the mechanical attributes and adhesive strength of SCE2 hydrogel. (A) Illustration of the hydrogel's adhesion process with tissue and the corresponding lap-shear examination. (B) The hydrogels' stress−strain profile obtained through lap-shear testing. (C) Illustrative depiction of conducting a tensile strength assessment. (D) Capturing the stress−strain relationship during the tensile evaluation of the hydrogels. (E–H) Analysis of SCE2 hydrogel's characteristics includes strain-responsive rheological behavior (E), frequency-responsive rheological properties (F), evaluations of step-strain (G), and shear-thinning attributes (H). Displaying SCE2 hydrogel's ease of injection through representative images. (I) Illustration of SCE2 hydrogel's injectability within a PBS setting. (J) A sequence of images showcasing the self-healing capabilities of the SCE2 hydrogel.

(Fig. 3C and D) experiments [38]. In comparison to SFMA hydrogel, which displayed fracture stress values at 27.45 kPa, both SCE0 and SCE2 hydrogels demonstrated superior fracture stress, especially SCE2 hydrogel, peaking at 64.37 kPa. During tension testing, SCE0 hydrogel's adhesive strength peaked at 18.13 kPa, and SCE2 hydrogel at 21.28 kPa. These figures were 2.93 and 3.44 times greater than SFMA hydrogel's 6.18 kPa, respectively. The heightened adhesion to tissues originates from the conversion of benzyl alcohol groups into benzaldehyde groups post-UV light exposure, resulting in the formation of Schiff base structures with the amino moieties on the tissue surface. Conclusively, SCE hydrogels showed superior adhesion capabilities compared to SMFA hydrogel, suggesting their potential as effective bioadhesives in clinical settings.

Next, we analyzed the rheological properties of SCE hydrogels.

Initially, strain scan tests were employed to investigate the hydrogel linear viscoelastic region, as shown in Fig. 3E. The gel point of the SCE2 hydrogel was found to be around 600 %, indicating it assumes a colloidal state at strains beyond this threshold. In these experiments, both hydrogels displayed phases where the G′ (storage modulus) consistently surpassed the G'' (loss modulus) [39]. Then, we assessed the frequency-dependent rheological characteristics of the hydrogels, as shown in Fig. 3F. The hydrogels' self-recovery properties were also investigated using dynamic amplitude experiments. Fig. 3G demonstrates the procedure where we initially subjected the hydrogel to a high strain (1000 %) to cause disintegration, followed by a low strain (1 %) to evaluate recovery ability. Under a 1000 % strain, there was a notable drop in G′, falling below G″, indicating network breakdown. However, on reverting to a 1 % strain, both G′ and G″ of SCE0 and SCE2 hydrogels

571

returned to their original values, demonstrating the SCE hydrogels' swift recovery capability. The hydrogel demonstrated excellent self-healing abilities through multiple sequential network breakdown and recovery cycles [40]. The foundation of SCE2 hydrogel's remarkable self-healing capability lies in the Schiff base reaction among polymer chains, creating dynamic and reversible cross-linking sites. Lastly, a shear test showed that the SCE2 hydrogel exhibited shear-thinning traits, indicating the hydrogel's prominent injectability (Fig. 3H) [41].

Additionally, we explored the macroscopic characteristics of the SCE hydrogels, focusing on their injectability and self-healing properties. We successfully created continuous hydrogel strips in a glass beaker filled with PBS using a 2 mL syringe (Fig. 3I). Subsequently, the SCE2 hydrogel was divided into two halves. Remarkably, these halves reunited within 30 min without external force, appearing almost identical to their original state (Fig. 3J). These observations support the superior mechanical properties of SCE2 hydrogel, implying its potential suitability for complex wound environments.

### 3.5. Intracellular antioxidant and biocompatibility abilities of SCE2 hydrogel

Biosafety is critical for using hydrogel materials as versatile dressings in tissue engineering [42,43]. With this in mind, we first assessed the cytocompatibility of the developed SCE hydrogels. To evaluate cell survival, the CCK-8 assay was used after RAW 264.7 macrophages and RS1 cells were cultured with extracts from SCE hydrogel for durations of 1, 3, and 5 days. Fig. 4A and B illustrate that cell viability in both SCE0 and SCE2 groups was above 80 %, indicating minimal toxicity of the developed SCE hydrogels. Fig. 4C shows that the supernatant from DDW, serving as a positive control, turned bright red, demonstrating red blood cell disruption [44]. Conversely, the PBS and SCE sets remained colorless with hemolysis rates below 5 %, demonstrating favorable hemocompatibility. On the third day of incubation, cells (RAW 264.7, RS1, and HGF) were stained using a calcein-AM/PI live/dead cell staining kit [45,46]. The intensity of green fluorescence in SCE hydrogel groups was nearly on par with the control set, and very few dead cells were detected in these SCE hydrogel groups (as seen in Fig. 4D and E; Fig. S10 in the Supporting Information). In summary, the developed SCE hydrogels showed outstanding biocompatibility and hemocompatibility, making them promising candidates as scaffold materials in biomedical engineering applications [47].

The hydrogel's antioxidant capability was verified at the cellular level. To begin with, a DCFH-DA fluorescent probe was employed for evaluating intracellular ROS levels, while also investigating the safeguarding impacts of SCE hydrogels within oxidative stress conditions. Results (Fig. 4F and G; Figs. S11–S14, Supporting Information) revealed that RAW 264.7, RS1, and HGF cells exposed to the $H_2O_2$ group exhibited heightened fluorescence, indicating elevated ROS levels. Contrastingly, cells in the SCE2 hydrogel group showed markedly reduced fluorescence, indicative of lower ROS levels. These findings align with flow cytometry results (Fig. 4H and I), which revealed increased green fluorescence in the $H_2O_2$ group and diminished DCFH-DA green fluorescence in the SCE hydrogel-treated set. Additionally, Fig. 4J and K indicated a significant reduction in cell growth due to oxidative damage following $H_2O_2$ exposure. However, cell survival rates notably improved in the SCE hydrogel-treated sets. For instance, RAW 264.7 and RS1 cells co-cultured with 670 μM $H_2O_2$ and SCE2 for 6 h exhibited cell survival rates of 61.16 % and 69.15 %, higher than the $H_2O_2$ and SCE0 hydrogel groups. These findings further substantiate SCE2 hydrogel's potent antioxidant capability in shielding cells against oxidative stress, highlighting its potential in wound healing applications.

### 3.6. Investigation of migration and angiogenesis of SCE2 hydrogel in vitro

To explore cell proliferation in oxidative stress conditions more

deeply, we conducted in vitro scratch assays. Using a pipette tip, we scratched the plate bottom containing RS1 cells and then treated with $H_2O_2$ and hydrogel. After 12 h and 24 h, we monitored the changes in the scratch area. As illustrated in Fig. 4L, the control group cells exhibited normal migration and proliferation with time, significantly reducing the migration distance after 24 h [48]. The scratch area in the $H_2O_2$ group remained largely unchanged, indicating minimal cell movement toward the scratches. On the other hand, the SCE2 group cells showcased better migration capabilities compared to the $H_2O_2$ group, leading to a gradual decrease in the scratch area. The leftover scratch area was a mere 34.7 % of the original area, implying that the formulated SCE2 could enhance cells' antioxidant capability by neutralizing exogenous oxidants (Fig. S15, Supporting Information).

Additionally, we used HUVECs to assess the influence of the newly developed SCE2 hydrogel on angiogenesis, especially under conditions of oxidative stress [49]. After incubation, HUVECs were arranged on Matrigel (Fig. 4M; Fig. S16, Supporting Information). The cells were then subjected to $H_2O_2$ and hydrogel treatment to monitor the development of HUVEC lumens in each group. After 8 h, HUVECs in the control group formed an interconnected tubular network with an increase in blood vessels and enhanced structural integrity [50]. In stark contrast, $H_2O_2$ significantly disrupted angiogenesis in HUVECs, with a complete lack of angiogenic activity. However, cells treated with SCE2 hydrogel showed close clustering and managed to establish a tubular network, implying that SCE2 hydrogel has the potential to mitigate ROS's harmful effects and maintain the angiogenic capability of HUVECs.

### 3.7. Assessing the photothermal antibacterial ability of SCE2 hydrogel

After evaluating the cellular level properties of the SCE2 hydrogels, we focused on assessing their photothermal antibacterial capabilities. Fig. 5A illustrates that the temperature of the SCE hydrogels rose more swiftly as the concentration of CFI increased. Specifically, a hydrogel with 0.5 mg/mL of CFI nanoparticles witnessed a solution temperature increase to 68.2 °C. When the CFI concentration was elevated to 2 mg/mL, the temperatures climbed to 87.2 °C. In a similar vein, escalating laser power densities led to higher temperatures when irradiating the SCE2 at a constant concentration (Fig. 5B). The hydrogel's thermal imagery, captured after 10 min of exposure at 808 nm, confirmed the observed temperature increase (Fig. S17, Supporting Information). To assess the photostability of the SCE hydrogels, we allowed them to cool down naturally after 10 min of light exposure. Fig. 5C reveals that there was no notable reduction in the temperature increase across four cycles of activating and deactivating the laser, indicating the hydrogel's superior photothermal stability. Moreover, the η of SCE2, a crucial metric reflecting the material's photothermal capability, was recorded at 46.3 % (Fig. 5D; Fig. S18, Supporting Information). This further indicates the exceptional photothermal capabilities of the designed SCE2 hydrogel.

Infection is a major factor hindering the process of wound healing [51]. In our study, we employed a plate counting method to measure the antibacterial effect of the SCE2 hydrogel, performing antibacterial experiments for both gram-negative (MRPA) and gram-positive (MRSA) bacteria in either the absence or presence of 808 nm NIR (Fig. 5E). The SCE hydrogels had little to no antimicrobial effect (Fig. S19, Supporting Information). As anticipated, the SCE2 + NIR group demonstrated an antibacterial effect close to 100 %, indicating that incorporating 808 nm NIR (1 W/cm$^2$ for 10 min) significantly enhanced the sterilizing efficacy of the SCE2.

To elucidate the potential antibacterial mechanism behind SCE hydrogels, we used SEM to inspect the detailed morphological alterations in bacteria. In the control group, MRSA and MRPA maintained their morphology with smooth bacterial cell membranes. The bacteria subjected to the SCE2 hydrogel + NIR laser experienced more extensive damage, such as ruptures or perforations in the cell membrane, affirming that the SCE2 hydrogel, aided by the photothermal effect of NIR
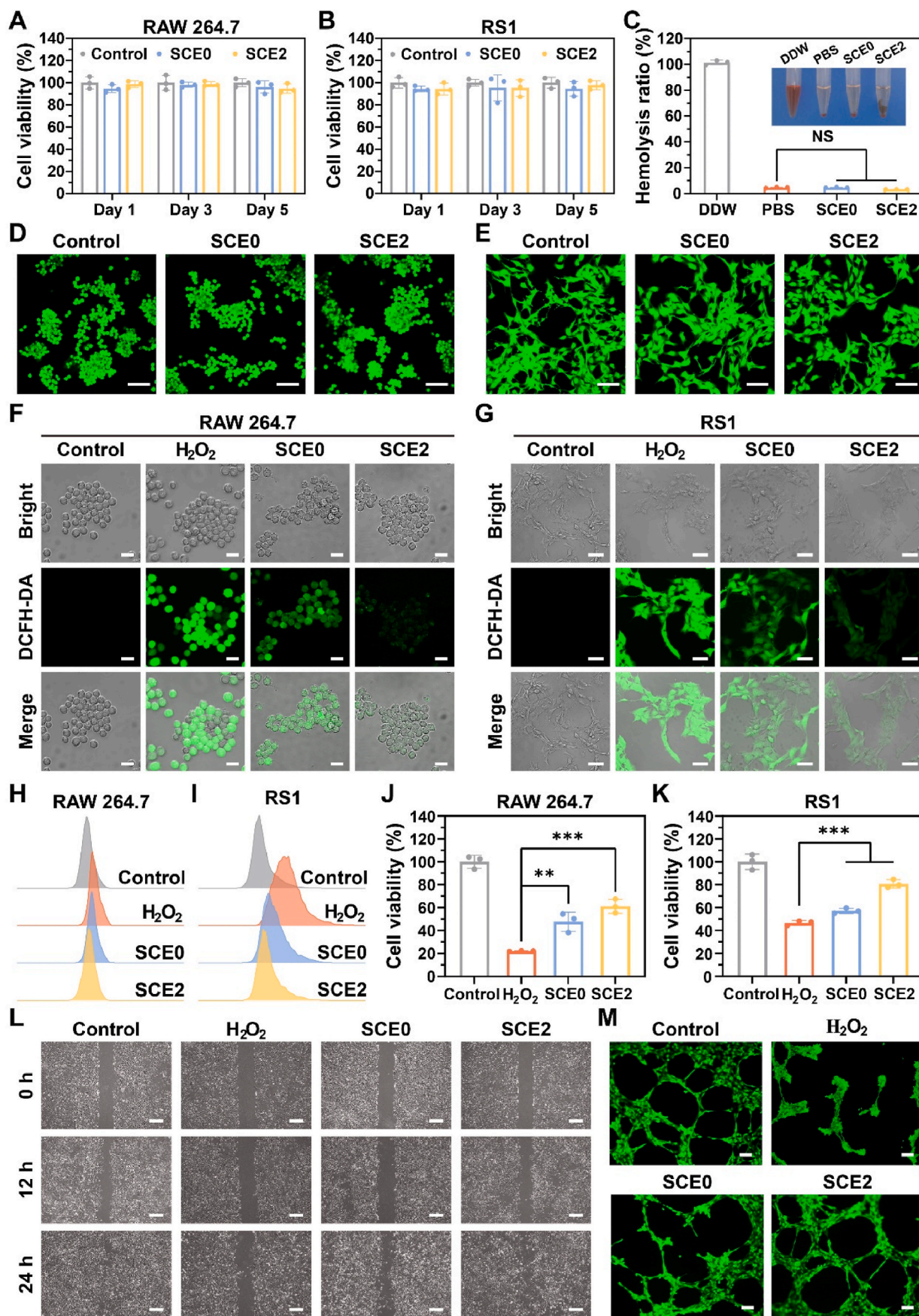
*(caption on next page)*

**Fig. 4.** In vitro cellular and hemolytic assays with SCE2 hydrogel. (A and B) Viability of RAW 264.7 macrophages (A) and RS1 cells (B) following exposure to PBS and SCE groups for durations of 1, 3, and 5 days. (C) Hemolysis assessment and images of SCE hydrogels post 2-h exposure to erythrocytes at 37 °C. (D and E) Fluorescence imaging of calcein-AM/PI staining in RAW 264.7 (D) and RS1 cells (E) after 3 days of varied treatments (scale bar: 100 μm). (F) Assessment of intracellular ROS neutralization by SCE hydrogels in RAW 264.7 cells employing DCFH-DA (scale bar: 20 μm). (G) Evaluation of ROS neutralization in RS1 cells by SCE hydrogels, indicated by DCFH-DA (scale bar: 50 μm). (H and I) Flow cytometric analysis of ROS in RAW 264.7 (H) and RS1 cells (I) using DCFH-DA as the detecting agent. (J and K) Survival rates of RAW 264.7 (J) and RS1 (K) cells post-incubation in SCE and $H_2O_2$ solution. (L) Images showing the migration of RS1 cells at intervals of 0, 12, and 24 h (scale bar: 300 μm). (M) Visuals captured through the fluorescence of HUVECs forming vessels (scale bar: 100 μm). Error bars represent the average ± standard deviation (n = 3). Levels of significance are denoted as *** for $P < 0.001$, ** for $P < 0.01$, * for $P < 0.05$, and NS for $P > 0.05$.

light, can enhance bacterial eradication.

Following that, a live/dead bacterial staining test was conducted to examine the bacterial cell membrane integrity, as seen in Fig. S20 in the Supporting Information. Compared to the control set, the group treated with SCE2 hydrogel had only a little red fluorescence, indicating essentially devoid bactericidal activity of SCE2 hydrogel. The strongest red PI fluorescence was detected in the group treated with SCE2 + NIR, indicating that PI penetrated the compromised bacterial membranes, coloring the bacteria red. Hence, SCE2 hydrogel showcases superior photothermal antibacterial capability and could serve as a robust antibacterial platform.

Furthermore, the architectural changes in bacteria underwent examination using TEM (Fig. 5F). Upon exposure to NIR light, MRSA and MRPA bacterial samples were gathered to assess morphological and structural characteristics via TEM. Contrary to the unexposed bacteria, which maintained a regular bacilliform shape with uniform nucleoplasm and a noticeable flagellum, the group treated with SCE2 + NIR exhibited significant alterations. Their cell walls thinned or vanished entirely, membranes wrinkled, and structural integrity was compromised. Additionally, bacterial swelling or shrinkage occurred, accompanied by membrane distortions, ruptures, and subsequent release of cellular contents.

### 3.8. Analysis of SCE2 hydrogel's therapeutic effectiveness via RNA sequencing

To delve deeper into the SCE2 hydrogel's inflammatory mechanism, we subjected the RAW 264.7macrophage cell line to IFN-γ and LPS stimulation, subsequently treating them with SCE2 hydrogel for gene expression alterations analysis through RNA sequencing. The resulting Venn diagram (Fig. 6A) revealed exclusivity in gene presence, with the M1 group having 3 unique genes, the SCE0 group showing 404 singular genes, and the SCE2 group presenting 447 individual genes. Further, sample integrity was assessed using Principal Component Analysis (PCA), which highlighted distinct distributions between the M1 and SCE2 groups, suggesting varied total gene expression profiles (Fig. 6B). Volcano diagrams indicated that 519 genes were markedly and differentially expressed; among them, 163 genes were heightened in expression, and 356 were suppressed (Fig. 6C). Analysis of these DEGs through Gene ontology (GO) revealed enriched biological processes such as cellular reaction to tumor necrosis factor and various immune and inflammatory responses (Fig. 6D).

To shed light on the cellular signaling mechanisms of SCE2 hydrogel in inflammatory therapy, both the Kyoto Encyclopedia of Genes and Genomes (KEGG) and Gene Ontology (GO) databases were employed for gene set enrichment analysis. The signaling pathway enrichment diagram from the KEGG database indicated changes in gene expression related to TNF, NF-kB, and IF-17 signaling pathways in the SCE2 group, as shown in Fig. 6E. Previous research has noted the function of ROS within the IL-17 signaling pathway. Activation of this pathway markedly increases the secretion of chemokines and pro-inflammatory cytokines like CCL2, TNF-α, and IL-1β. It also shifts macrophages towards the pro-inflammatory M1 subtype and stimulates neutrophil recruitment and activation. Remarkably, SCE2 hydrogel mitigates inflammation by neutralizing ROS and suppressing IL-17 signaling pathway activities.

Gene expression disparities between the M1 and SCE2 groups were depicted in a heatmap (Fig. 6F). Post-treatment with SCE2 hydrogel, a

notable upregulation was observed in several critical pro-inflammatory genes, including CCL5, IL-6, CCL3, S100A8, and NOS2. As displayed in Fig. 6G–a chord diagram displayed the diminished gene expression and linked GO biological processes, including the control of inflammation, angiogenesis, immune responses, and improved regulation of apoptosis. To unravel the specific pathways influenced by SCE2, further investigation was conducted through gene set enrichment analysis (GSEA), as displayed in Fig. 6H. These findings indicated a reduction in TNF and NOD-like receptor signaling pathways in macrophages after SCE2 hydrogel application. Collectively, the data robustly suggest that the administration of SCE2 hydrogel significantly promotes wound healing by attenuating oxidative stress and curbing inflammatory responses.

### 3.9. In vivo healing of MRSA-infected diabetic back skin wounds by SCE2 hydrogel

Following the acquisition of in vitro results, our investigation shifted to analyzing the in vivo back skin wound healing performance of the SCE2 hydrogel. Initially, we focused on determining the hemostatic efficacy of SCE2 hydrogels. In the event of a wound, swift hemostasis plays a crucial role in ensuring a repair of superior quality. To facilitate this, we incorporated NB groups with photo-triggered adhesive features into the hydrogel's matrix, with the objective of enabling the dressings to promptly control bleeding. The SCE2 hydrogel's hemostatic effectiveness was appraised using both a tail model and a liver model. Within the liver hemostasis model (Fig. S21, Supporting Information), groups treated with the hydrogel exhibited the most pronounced hemostatic effect, displaying almost no apparent bleeding in contrast to the noticeable hemorrhage observed in other groups. This conclusion was echoed in the tail hemostasis model, further substantiating SCE2 hydrogel's remarkable capacity for in vivo bleeding cessation. Quantitative analysis revealed that blood loss in the untreated control (139.53 mg) and gauze-applied (98.73 mg) groups were significantly higher compared to the SCE2 hydrogel group (34.7 mg) (Figs. S22 and S23, Supporting Information).

Following that, we explored the SCE2 hydrogel's capabilities in photothermal heating and sterilization. After a 3-min exposure to the NIR laser, the temperature at the rat wound sites treated with PBS and SCE0 remained relatively unchanged (Fig. S24, Supporting Information). In contrast, for the SCE2 + NIR group, the temperature notably rose from 36.8 °C to 60.7 °C. We then collected and quantified bacteria from the wound sites post-treatment using an agar plate method (Fig. S25, Supporting Information). Aligning with the in vitro findings of hydrogel's antimicrobial efficacy, the control and 3 M groups exhibited the highest bacterial counts. Meanwhile, the SCE0 and SCE2 groups showed moderate bacterial presence, and notably, the SCE2 + NIR group recorded the lowest bacterial count. These observations collectively indicate that the SCE2 hydrogel, when aided by NIR, demonstrated superior antibacterial effectiveness.

Subsequently, the healing properties of the developed SCE2 hydrogel were evaluated using a MRSA-infected diabetic rat back skin wound model. Wound progression was documented through photographs taken on days 0, 3, 7, and 14, as presented in Fig. 7A. The wound closure in diabetic rats treated with SCE0, SCE2, and SCE2 + NIR occurred more rapidly compared to those receiving PBS and 3 M treatments (Fig. 7B). Notably, after 14 days of treatment, a significant wound remained in the 3 M hydrogel-treated group (wound area = 31.3 %), similar to the PBS-
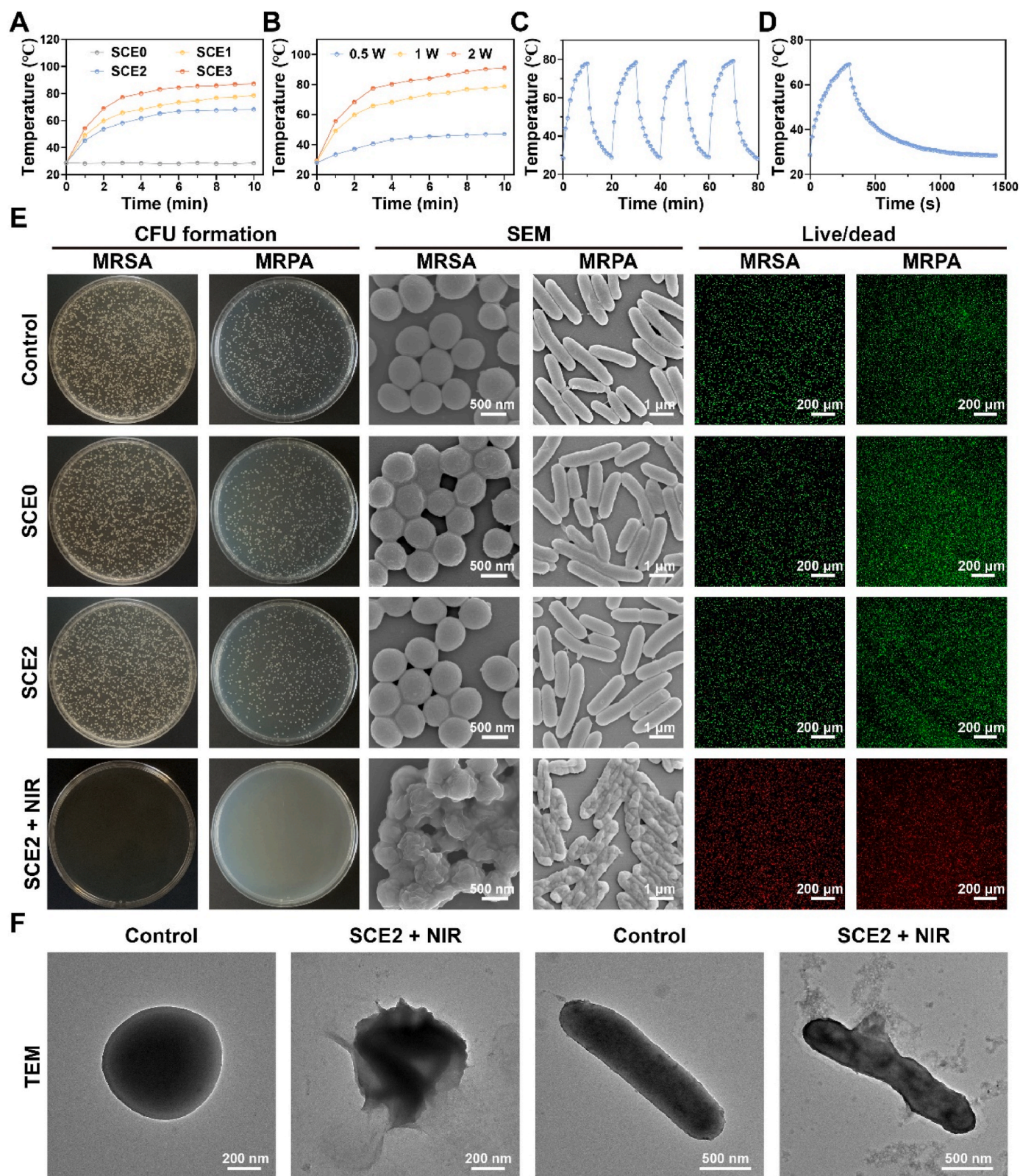
**Fig. 5.** Examining the SCE2 hydrogel's in vitro photothermal antibacterial properties (A) Analyzing the temperature rise patterns among various hydrogels. (B) Studying the thermal increase in SCE2 hydrogel under different NIR light exposures. (C) Investigating the photothermal resilience of SCE2 hydrogel through four alternating heating and cooling cycles. (D) Analyzing the heating and cooling phases of SCE2 hydrogel's photothermal process. (E) Assessing SCE2 hydrogel's antibacterial effectiveness against MRSA and MRPA through methods like agar plate counting, SEM, and bacterial live-dead staining. (F) Presenting TEM imagery of bacteria pre and post exposure to SCE2 hydrogel combined with NIR treatment.
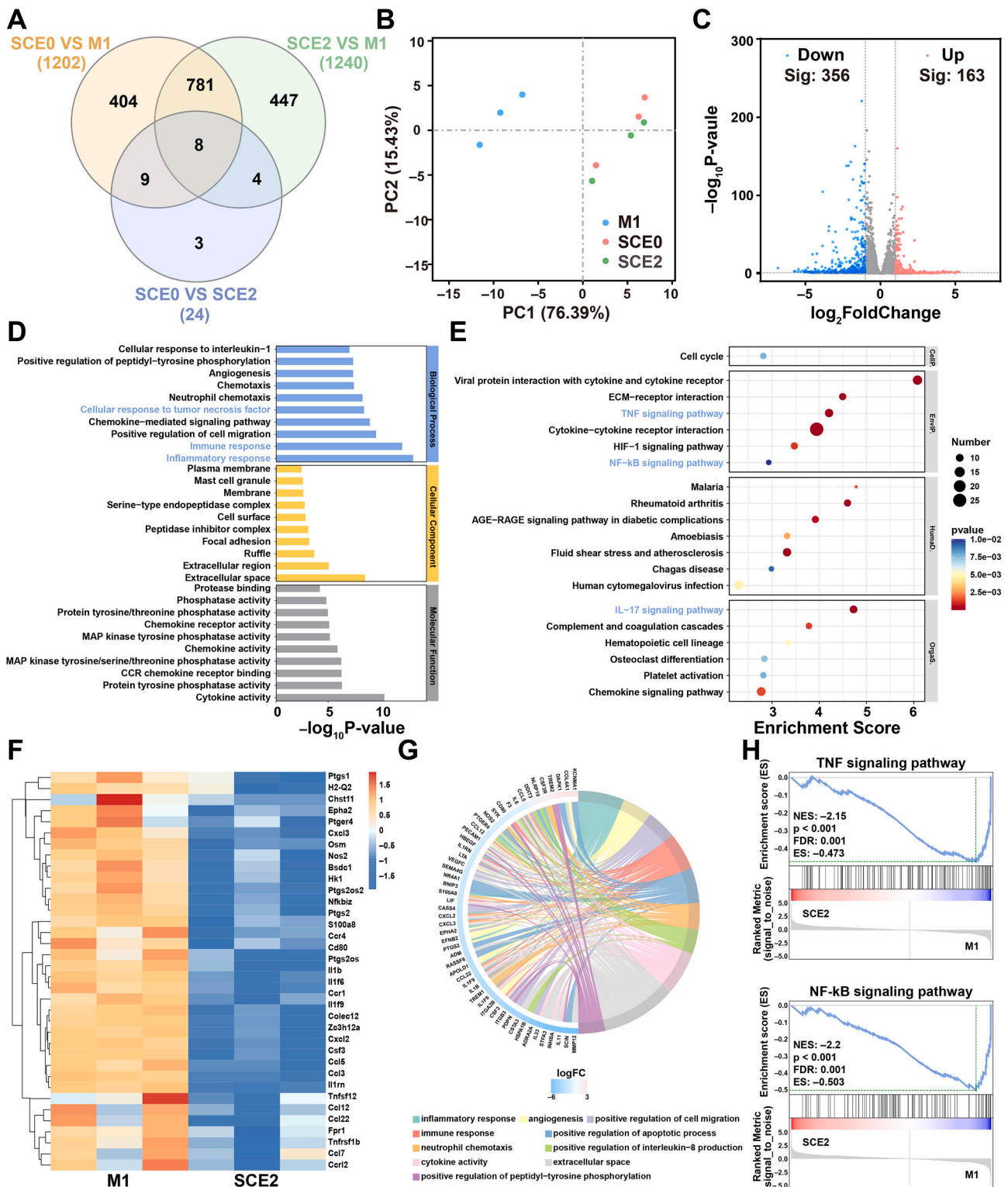
**Fig. 6.** RNA sequencing evaluation of SCE2 hydrogel's therapeutic efficacy. (A) Differential gene count comparison in a Venn diagram for M1, SCE0, and SCE2 categories. (B) Three-group PCA plot illustrating proteomic data with three biological replicates per group. (C) Volcano chart presenting the downregulated and upregulated gene expressions in the SCE2 versus M1 gene expressions. (D) Analysis of GO pathways enriched among detected DEGs. (E) Dot chart depicting selected DEGs' KEGG enrichment analysis outcomes between M1 and SCE2 groups. (F) Heat map representing downregulated genes in both M1 and SCE2 groups. (G) Chord diagram illustrating GO enrichment terms linked to specific downregulated genes associated with oxidative stress. (H) GSEA results indicating cytosolic TNF and NF-kB signaling pathways' gene set enrichment in cells treated with SCE2 hydrogel.
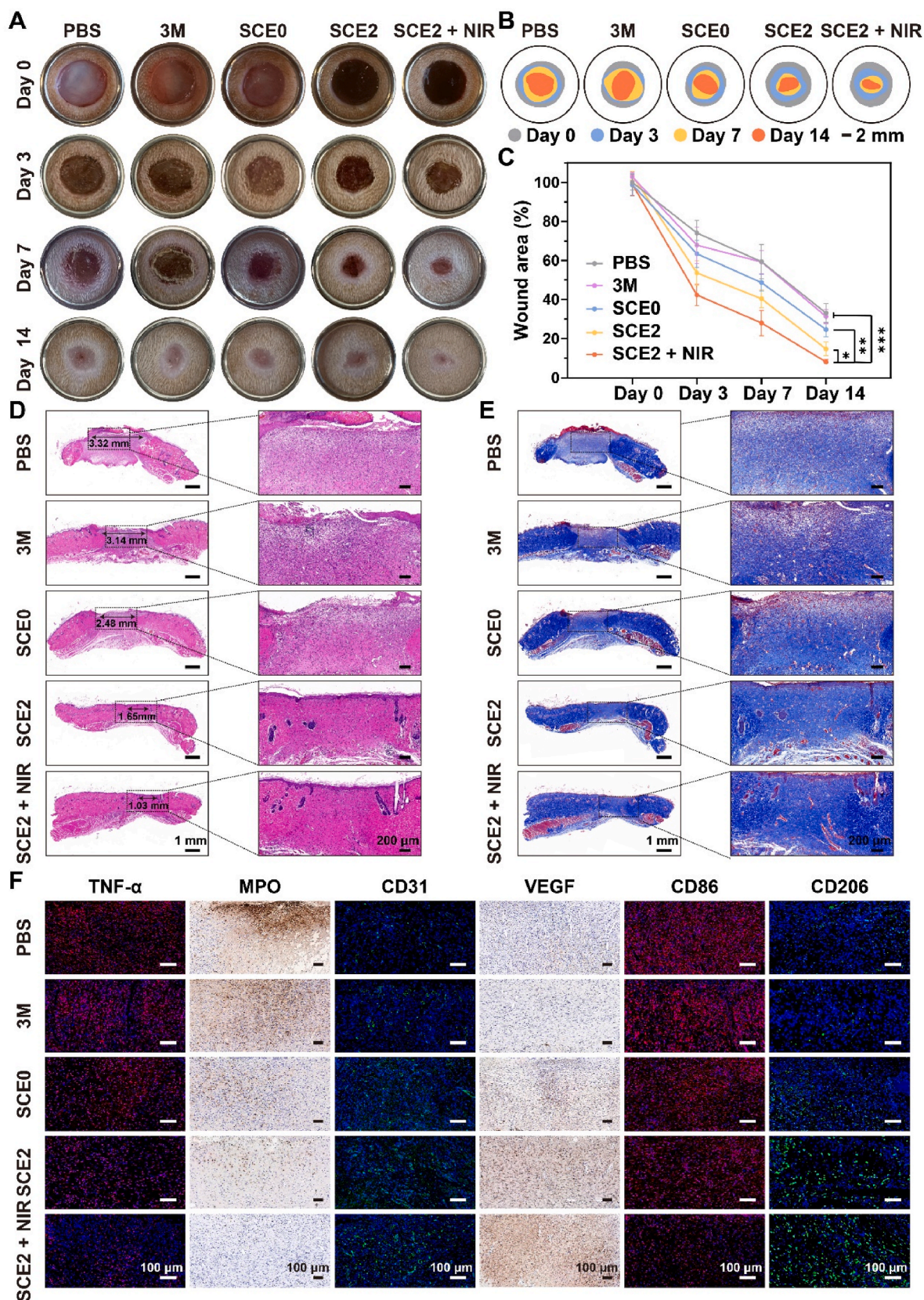
**Fig. 7.** Assessment of SCE2 hydrogel's therapeutic efficacy on back skin wounds in diabetic rats. (A) Depictions of skin injury progression in PBS, 3 M, SCE0, SCE2, and SCE2 + NIR. (B) Visual representation of healing stages in wounds. (C) Comparative measurement of wound sizes in all groups. (D–F) Staining for histology in rat skin sections from the wound region: H&E (D), Masson's trichrome (E), and markers TNF-α, MPO, CD31, VEGF, CD86, and CD206 (F). Error bars represent the average ± standard deviation (n = 3).

treated group (wound area = 33.1 %), suggesting that 3 M hydrogel is less effective in healing bacterially infected wounds. In contrast, the SCE0 and SCE2 hydrogels exhibited considerable decreases in the wound area, reaching 24.6 % and 14.8 % after 14 days, demonstrating their efficacy in expediting wound healing. Remarkably, the SCE2 + NIR group accomplished near-total wound healing, exhibiting an average wound area of merely 8.1 % at the conclusion of the monitoring period, as elaborated in Fig. 7C.

Moreover, fourteen days post-surgery, we collected the wounds for histological examination, as depicted in Fig. 7D. The SCE2 + NIR group exhibited markedly better healing than the PBS group. The newly regenerated skin in this group showcased complete epithelial and dermal structures, alongside a notable increase in new blood vessels and hair follicle formation. We then used Masson staining to assess collagen regeneration [52]. In the SCE2 + NIR group, there was a noticeable presence of dense and orderly aligned collagen fibers, as depicted in Fig. 7E, indicative of enhanced collagen production [53]. Furthermore, TNF-α staining was conducted. Fig. 7F shows pronounced inflammation in the control set, while the SCE2 + NIR set displayed lower TNF-α levels compared to both SCE0 and SCE2 hydrogel groups [54]. This observation gains additional support from MPO staining of neutrophils, demonstrating the minimal inflammatory response in the SCE2 + NIR group, as evidenced in Figs. S26A and S26B in the Supporting Information.

Furthermore, we employed CD31 and VEGF staining to assess neovascularization. Fig. 7F shows that the SCE2 + NIR group had significantly more new blood vessel proliferation than the PBS group, as further detailed in Figs. S27A and S27B in the Supporting Information [55]. Consistent with results from the rat back skin wound experiments, the SCE2 + NIR set possessed the least CD86 expression and the highest CD206 expression, as evidenced in Fig. 7F and S28 in the Supporting Information. The SCE2 hydrogel enhanced with NIR contributed to a reduction in M1 macrophages and an increase in M2 macrophages, thus promoting the production of proteins related to anti-inflammatory and angiogenic cellular factors. This contributed significantly to the accelerated healing of MRSA-infected back skin trauma.

### 3.10. In vivo healing of MRSA-infected diabetic oral ulcer wounds by SCE2 hydrogel

After confirming the SCE2 hydrogel's ability to repair wounds on dorsal skin, a model for oral ulcers was subsequently developed to further evaluate its healing efficacy (Fig. 8A and B). The detailed process for constructing the model is shown in Fig. 8A. When a chemical reaction was induced in the rat mucosa using glacial acetic acid, an immediate reaction occurred at the application site, marked by swift whitening of the mucosa. Besides the sets receiving hydrogel treatments, the negative control was subjected to PBS administration, and the positive control involved treatment with a glucocorticoid solution containing dexamethasone (DEX). Fig. 8B shows a clearly defined, hardened central ulcer in the oral cavity of each rat immediately following surgery. By the second day, this ulcer became increasingly noticeable, with the adjacent mucosa appearing swollen, reddened, and coated by a yellowish pseudomembrane. Two days following the commencement of hydrogel therapy, we noted a reduction in both the thickness of the pseudomembrane and the size of the ulcer area. After four days, a small section of the pseudomembrane remained within the PBS group. Conversely, the DEX and SCE2 sets showed decreased swelling and redness in the surrounding mucosal area, with the ulcer size being notably smaller in the SCE2 + NIR set. By day five, the oral ulcers in the SCE2 + NIR set had virtually healed.

Subsequently, on the fifth day, samples of wounds from the oral region were collected for comprehensive histological and morphological analysis. Fig. 8C reveals that the epidermis in both PBS and DEX groups showed signs of necrosis and peeling, with significant infiltration of inflammatory cells. In contrast, the SCE2 set exhibited decreased

infiltration of such cells along with a modest enhancement in fibroblast proliferation. Furthermore, the SCE2 + NIR set displayed a fully intact epithelial layer with barely any connective tissue presence in the submucosal area. Regarding Masson's trichrome staining (Fig. 8D), the SCE2 + NIR group displayed the most prominent collagen deposition, characterized by dense, orderly fibers. Immunohistochemical analysis was then employed to assess mucosal inflammation in each group. TNF-α expression was notably higher in both the SCE0 hydrogel and DEX sets, comparatively lower in the SCE2 set, and least in the SCE2 + NIR set. This pattern suggests that treatment with SCE2 + NIR effectively reduced inflammation in the ulcerated area, as shown in Fig. S29A of the Supporting Information. Additionally, MPO staining for neutrophils corroborated the minimal inflammatory response in the SCE2 + NIR group, as detailed in Fig. S29B in the Supporting Information.

Additionally, CD31 and VEGF stains were employed to assess new blood vessel growth. Fig. 8E demonstrated a significantly higher growth of new vessels in the SCE2 + NIR compared to others (Fig. S30, Supporting Information). Neovascularization plays a vital role in providing nutrients and oxygen to wounds with high metabolic demands, thus aiding in the development of granulation tissue. Similar to findings in rat back skin injuries, therapy with SCE2 + NIR demonstrated the least expression of CD86 and the most pronounced expression of CD206 (Fig. S31, Supporting Information). As M1 macrophages decreased and M2 macrophages increased, SCE2 hydrogel enhanced by NIR encouraged the production of proteins related to anti-inflammatory and angiogenic cells, leading to the accelerated healing of oral sores.

Ultimately, we examined the biosafety of the developed SCE2 hydrogel dressings, a crucial factor in determining their suitability for wound care. We began by performing blood biochemical tests following different treatments. The results showed no notable differences between subjects treated with the SCE2 hydrogel and the control group, indicating that the SCE2 hydrogel is biocompatible with blood (Fig. S32, Supporting Information). Furthermore, H&E methods were employed to assess the SCE2 hydrogel's potential organ toxicity in rats. Relative to healthy, untreated tissues, organs from rats that received hydrogel treatment showed no significant infiltration of inflammatory cells (Fig. S33, Supporting Information). Such findings suggest that the SCE2 hydrogel exhibits minimal biological toxicity toward healthy in vivo tissues. Together, these findings emphasize the SCE2 hydrogel's favorable safety profile, making it a suitable candidate for clinical applications in treating oral wounds.

### 4. Conclusions

In summary, our research presents the approach of using SCE2 hydrogel for developing an immunomodulatory patch that attaches to the oral mucosa. This patch is composed of methacrylate silk fibroin, nitrobenzyl-modified chondroitin sulfate, and nanoparticles derived from cuttlefish ink, designed to improve both the duration of adhesion and healing efficiency under wet conditions. As expected, exposure to ultraviolet light leads to the formation of a sticky hydrogel layer over mucosal injuries. Subsequently, the SCE2's orderly release of bioactive substances provides antibacterial, anti-inflammatory, and antioxidative benefits, significantly enhancing treatment outcomes for oral mucosal defects. Additionally, the SCE2 patch is entirely absorbable by the body and exhibits negligible toxicity after serving its intended purpose. Using a streptozotocin-induced diabetic rat model, the SCE2 hydrogel's ability to facilitate the repair of dorsal skin injuries and oral ulcers was validated. We foresee that the SCE2 platform presented in this study will advance the development of tissue adhesives and motivate the creation of wound dressings using naturally derived bioactive substances.

### Ethics approval and consent to participate

The research involving animals was conducted in strict compliance with the guidelines and standards established by the Wenzhou Medical
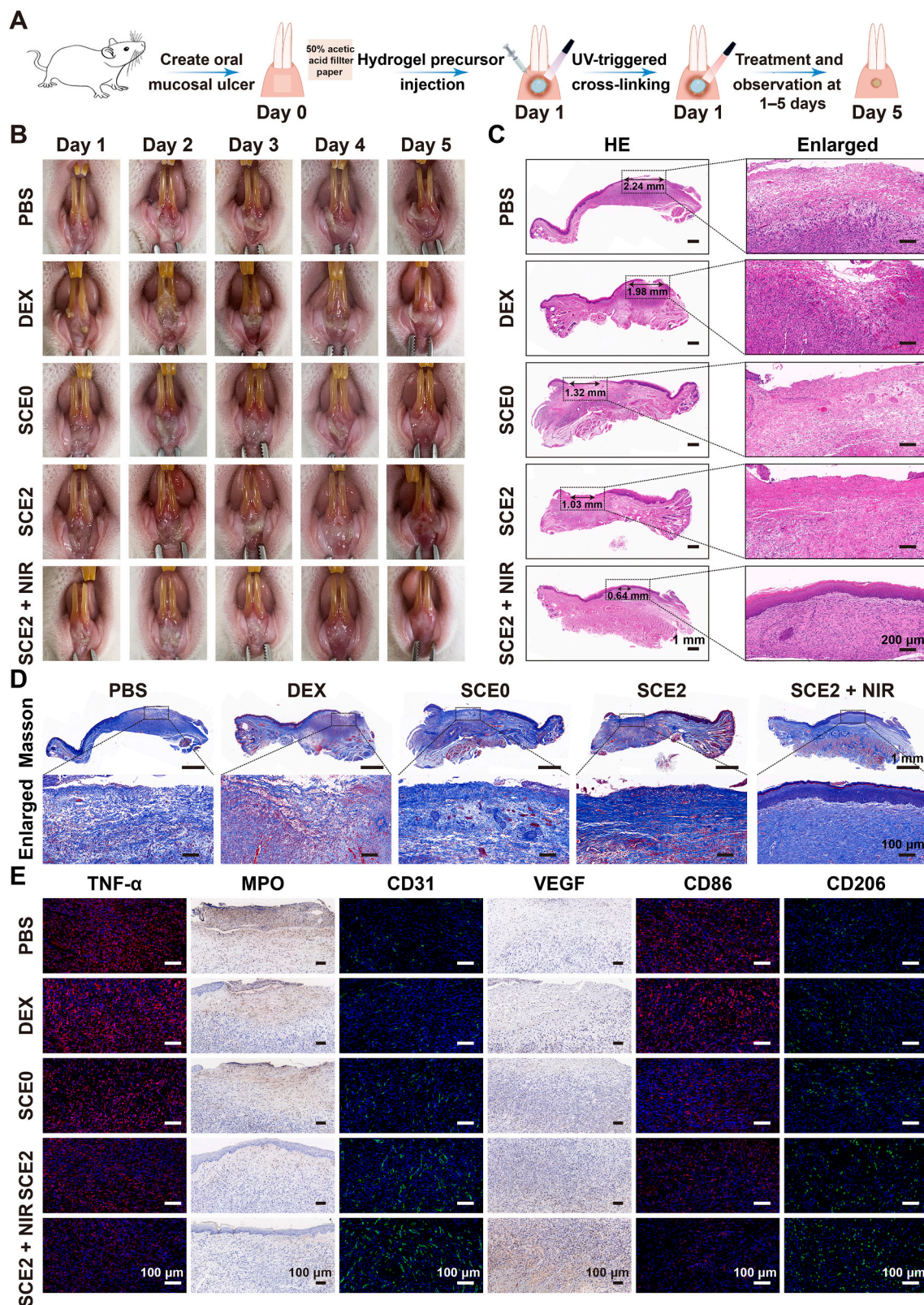
**Fig. 8.** Assessment of SCE2 hydrogel's therapeutic efficacy on oral ulcer wounds in type 1 diabetic rats. (A) Diagram illustrating the creation and treatment approach for oral ulcers. (B) Digital images showing oral ulcer healing in PBS, DEX, SCE2, and SCE2 + NIR sets throughout 1–5 days. (C–E) Stained sections of oral ulcer wounds: H&E (C), Masson's trichrome (D), and markers TNF-α, MPO, CD31, VEGF, CD86, and CD206 (E).

University's Institutional Animal Care and Use Committee, which approved the authorization number Wydw7019-0134.

## Declaration of interests statement

## CRediT authorship contribution statement

**Yajing Xiang:** Writing – original draft, Software, Methodology, Investigation, Data curation. **Zhuge Pan:** Formal analysis. **Xiaoliang Qi:** Writing – review & editing, Conceptualization. **XinXin Ge:** Software. **Junbo Xiang:** Methodology. **Hangbin Xu:** Data curation. **Erya Cai:** Validation. **Yulong Lan:** Data curation. **Xiaojing Chen:** Data curation. **Ying Li:** Software. **Yizuo Shi:** Validation. **Jianliang Shen:** Supervision. **Jinsong Liu:** Visualization.

## Acknowledgements

## Appendix A. Supplementary data

Supplementary data to this article can be found online at https://doi.org/10.1016/j.bioactmat.2024.04.022.

## References

[1] S. Choi, J. Jeon, Y. Bae, Y. Hwang, S.W. Cho, Mucoadhesive phenolic pectin hydrogels for saliva substitute and oral patch, Adv. Funct. Mater. 33 (44) (2023) 2303043.

[2] C. Cui, L. Mei, D. Wang, P. Jia, Q. Zhou, W. Liu, A self-stabilized and water-responsive deliverable coenzyme-based polymer binary elastomer adhesive patch for treating oral ulcer, Nat. Commun. 14 (1) (2023) 7707.

[3] J.G. Edmans, B. Ollington, H.E. Colley, M.E. Santocildes-Romero, L. Siim Madsen, P.V. Hatton, S.G. Spain, C. Murdoch, Electrospun patch delivery of anti-TNFalpha F (ab) for the treatment of inflammatory oral mucosal disease, J. Contr. Release 350 (2022) 146–157.

[4] E. Mohammed, A.G. Aboulkhair, M.M. Tawifq, Effect of nano-chitosan and nano-doxycycline gel on healing of induced oral ulcer in rat model: histological and immunohistochemical study, Clin. Oral Invest. 26 (3) (2021) 3109–3118.

[5] J. Wu, Z. Pan, Z.Y. Zhao, M.H. Wang, L. Dong, H.L. Gao, C.Y. Liu, P. Zhou, L. Chen, C.J. Shi, Z.Y. Zhang, C. Yang, S.H. Yu, D.H. Zou, Anti-swelling, robust, and adhesive extracellular matrix-mimicking hydrogel used as intraoral dressing, Adv. Mater. 34 (20) (2022) 2200115.

[6] P. Makvandi, U. Josic, M. Delfi, F. Pinelli, V. Jahed, E. Kaya, M. Ashrafizadeh, A. Zarepour, F. Rossi, A. Zarrabi, T. Agarwal, E.N. Zare, M. Ghomi, T. Kumar Maiti, L. Breschi, F.R. Tay, Drug delivery (Nano)Platforms for oral and dental applications: tissue regeneration, infection control, and Cancer management, Adv. Sci. 8 (8) (2021) 2004014.

[7] N. Samiraninezhad, K. Asadi, H. Rezazadeh, A. Gholami, Using chitosan, hyaluronic acid, alginate, and gelatin-based smart biological hydrogels for drug delivery in oral mucosal lesions: a review, Int. J. Biol. Macromol. 252 (2023) 126573.

[8] M. Mehravaran, A. Haeri, S. Rabbani, S.A. Mortazavi, M. Torshabi, Preparation and characterization of benzydamine hydrochloride-loaded lyophilized mucoadhesive wafers for the treatment of oral mucositis, J. Drug Deliv. Sci. Tech. 78 (2022) 103944.

[9] V. Hearnden, V. Sankar, K. Hull, D.V. Juras, M. Greenberg, A.R. Kerr, P. B. Lockhart, L.L. Patton, S. Porter, M.H. Thornhill, New developments and opportunities in oral mucosal drug delivery for local and systemic disease, Adv. Drug Deliver. Rev. 64 (1) (2012) 16–28.

[10] W. Li, L. Jiang, S. Wu, S. Yang, L. Ren, B. Cheng, J. Xia, A shape-Programmable hierarchical fibrous membrane composite system to promote wound healing in diabetic patients, Small 18 (11) (2022) 2107544.

[11] C. Jumelle, A. Yung, E.S. Sani, Y. Taketani, F. Gantin, L. Bourel, S. Wang, E. Yuksel, S. Seneca, N. Annabi, R. Dana, Development and characterization of a hydrogel-based adhesive patch for sealing open-globe injuries, Acta Biomater. 137 (2022) 53–63.

[12] J.H. Ryu, J.S. Choi, E. Park, M.R. Eom, S. Jo, M.S. Lee, S.K. Kwon, H. Lee, Chitosan oral patches inspired by mussel adhesion, J. Contr. Release 317 (2020) 57–66.

[13] Y. Jiang, X. Zhang, W. Zhang, M. Wang, Y. Lan, K. Wang, L. Han, X. Lu, Infant skin friendly adhesive hydrogel patch activated at body temperature for bioelectronics securing and diabetic wound healing, ACS Nano 16 (6) (2022) 8662–8676.

[14] S. Hu, X. Pei, L. Duan, Z. Zhu, Y. Liu, J. Chen, T. Chen, P. Ji, Q. Wan, J. Wang, A mussel-inspired film for adhesion to wet buccal tissue and efficient buccal drug delivery, Nat. Commun. 12 (1) (2021) 1689.

[15] Y. Zhao, S. Song, X. Ren, J. Zhang, Q. Lin, Y. Zhao, Supramolecular adhesive hydrogels for tissue engineering applications, Chem. Rev. 122 (6) (2022) 5604–5640.

[16] A.Z. Abo-shady, H. Elkammar, V.S. Elwazzan, M. Nasr, Formulation and clinical evaluation of mucoadhesive buccal films containing hyaluronic acid for treatment of aphthous ulcer, J. Drug Deliv. Sci. Technol. 55 (2020) 101442.

[17] Q. Mao, Z. Huang, Y. Zhang, Q. Chen, K. Jiang, Y. Hong, H. Ouyang, Y. Liang, A strong adhesive biological hydrogel for colon leakage repair and abdominal adhesion prevention, Adv. Healthcare Mater. 12 (28) (2023) 2301379.

[18] F. Wang, W. Zhang, Y. Qiao, D. Shi, L. Hu, J. Cheng, J. Wu, L. Zhao, D. Li, W. Shi, L. Xie, Q. Zhou, ECM-like adhesive hydrogel for the regeneration of large corneal stromal defects, Adv. Healthcare Mater. 12 (21) (2023) 2300192.

[19] J. Zhu, H. Zhou, E.M. Gerhard, S. Zhang, F.I. Parra Rodriguez, T. Pan, H. Yang, Y. Lin, J. Yang, H. Cheng, Smart bioadhesives for wound healing and closure, Bioact. Mater. 19 (2023) 360–375.

[20] A.P. Dhand, J.H. Galarraga, J.A. Burdick, Enhancing biopolymer hydrogel functionality through interpenetrating networks, Trends Biotechnol. 39 (5) (2021) 519–538.

[21] R. Iglesias-Bartolome, A. Uchiyama, A.A. Molinolo, L. Abusleme, S.R. Brooks, J. L. Callejas-Valera, D. Edwards, C. Doci, M.L. Asselin-Labat, M.W. Onaitis, N. M. Moutsopoulos, J.S. Gutkind, M.I. Morasso, Transcriptional signature primes human oral mucosa for rapid wound healing, Sci. Transl. Med. 10 (451) (2018) eaap8798.

[22] W. Zhou, Z. Duan, J. Zhao, R. Fu, C. Zhu, D. Fan, Glucose and MMP-9 dual-responsive hydrogel with temperature sensitive self-adaptive shape and controlled drug release accelerates diabetic wound healing, Bioact. Mater. 17 (2022) 1–17.

[23] S. Şenel, A.I. Özdoğan, G. Akca, Current status and future of delivery systems for prevention and treatment of infections in the oral cavity, Drug Deliv. Transl. Res. 11 (4) (2021) 1703–1734.

[24] F. Chen, X. Liu, X. Ge, Y. Wang, Z. Zhao, X. Zhang, G.-Q. Chen, Y. Sun, Porous polydroxyalkanoates (PHA) scaffolds with antibacterial property for oral soft tissue regeneration, Chem. Eng. J. 451 (2023) 138899.

[25] A. Abdollahi, A. Malek-Khatabi, M.S. Razavi, M. Sheikhi, K. Abbaspour, Z. Rezagholi, A. Atashi, M. Rahimzadegan, M. Sadeghi, H.A. Javar, The recent advancement in the chitosan-based thermosensitive hydrogel for tissue regeneration, J. Drug Deliv. Sci. Tech. 86 (2023) 104627.

[26] X. Lu, S. Shi, H. Li, E. Gerhard, Z. Lu, X. Tan, W. Li, K.M. Rahn, D. Xie, G. Xu, F. Zou, X. Bai, J. Guo, J. Yang, Magnesium oxide-crosslinked low-swelling citrate-based mussel-inspired tissue adhesives, Biomaterials 232 (2020) 119719.

[27] X. Cao, L. Sun, D. Xu, S. Miao, N. Li, Y. Zhao, Melanin-integrated structural color hybrid hydrogels for wound healing, Adv. Sci. 10 (22) (2023) 2300902.

[28] H. Mao, S. Zhao, Y. He, M. Feng, L. Wu, Y. He, Z. Gu, Multifunctional polysaccharide hydrogels for skin wound healing prepared by photoinitiator-free crosslinking, Carbohydr. Polym. 285 (2022) 119254.

[29] J.K. Sahoo, O. Hasturk, T. Falcucci, D.L. Kaplan, Silk chemistry and biomedical material designs, Nat. Rev. Chem 7 (5) (2023) 302–318.

[30] A. Fathi, M. Gholami, H. Motasadizadeh, A. Malek-Khatabi, R. Sedghi, R. Dinarvand, Thermoresponsive in situ forming and self-healing double-network hydrogels as injectable dressings for silymarin/levofloxacin delivery for treatment of third-degree burn wounds, Carbohydr. Polym. 331 (2024) 121856.

[31] X. Qi, Y. Xiang, E. Cai, S. You, T. Gao, Y. Lan, H. Deng, Z. Li, R. Hu, J. Shen, All-in-one: harnessing multifunctional injectable natural hydrogels for ordered therapy of bacteria-infected diabetic wounds, Chem. Eng. J. 439 (2022) 135691.

[32] W.Q. Qu, J.X. Fan, D.W. Zheng, H.Y. Gu, Y.F. Yu, X. Yan, K. Zhao, Z.B. Hu, B.W. Qi, X.Z. Zhang, A.X. Yu, Deep-penetration functionalized cuttlefish ink nanoparticles for combating wound infections with synergetic photothermal-immunologic therapy, Biomaterials 301 (2023) 122231.

[33] D. Wang, M.L. Kuzma, X. Tan, T.C. He, C. Dong, Z. Liu, J. Yang, Phototherapy and optical waveguides for the treatment of infection, Adv. Drug Deliv. Rev. 179 (2021) 114036.

[34] M. Ghovvati, S. Baghdasarian, A. Baidya, J. Dhal, N. Annabi, Engineering a highly elastic bioadhesive for sealing soft and dynamic tissues, J. Biomed. Mater. Res. B Appl. Biomater. 110 (7) (2022) 1511–1522.

[35] J. Zhang, Y. Zheng, J. Lee, J. Hua, S. Li, A. Panchamukhi, J. Yue, X. Gou, Z. Xia, L. Zhu, X. Wu, A pulsatile release platform based on photo-induced imine-crosslinking hydrogel promotes scarless wound healing, Nat. Commun. 12 (1) (2021) 1670.

[36] B. Kong, Y. Chen, R. Liu, X. Liu, C. Liu, Z. Shao, L. Xiong, X. Liu, W. Sun, S. Mi, Fiber reinforced GelMA hydrogel to induce the regeneration of corneal stroma, Nat. Commun. 11 (1) (2020) 1435.

[37] Y. Zhang, M. Li, Y. Wang, F. Han, K. Shen, L. Luo, Y. Li, Y. Jia, J. Zhang, W. Cai, K. Wang, M. Zhao, J. Wang, X. Gao, C. Tian, B. Guo, D. Hu, Exosome/metformin-loaded self-healing conductive hydrogel rescues microvascular dysfunction and

promotes chronic diabetic wound healing by inhibiting mitochondrial fission, Bioact. Mater. 26 (2023) 323–336.

[38] Y. Zheng, K. Shariati, M. Ghovvati, S. Vo, N. Origer, T. Imahori, N. Kaneko, N. Annabi, Hemostatic patch with ultra-strengthened mechanical properties for efficient adhesion to wet surfaces, Biomaterials 301 (2023) 122240.

[39] B. Kong, R. Liu, X. Hu, M. Li, X. Zhou, Y. Zhao, T. Kong, Cornea-Inspired ultrasound-responsive adhesive hydrogel patches for keratitis treatment, Adv. Funct. Mater. 34 (12) (2023) 2310544.

[40] S. Maiz-Fernández, L. Pérez-Álvarez, L. Ruiz-Rubio, J.L. Vilas-Vilela, S. Lanceros-Mendez, Polysaccharide-based in situ self-healing hydrogels for tissue engineering applications, Polymers–Basel 12 (10) (2020) 2261.

[41] S. Gholizadeh, X. Chen, A. Yung, A. Naderi, M. Ghovvati, Y. Liu, A. Farzad, A. Mostafavi, R. Dana, N. Annabi, Development and optimization of an ocular hydrogel adhesive patch using definitive screening design (DSD), Biomater. Sci. 11 (4) (2023) 1318–1334.

[42] M. Ghovvati, K. Bolouri, L. Guo, N. Kaneko, X. Jin, Y. Xu, Z. Hua, Y. Lei, Harnessing the power of electroconductive polymers for breakthroughs in tissue engineering and regenerative medicine, Mater. Chem. Horiz. 2 (3) (2023) 195–206.

[43] Y. Xiang, X. Qi, E. Cai, C. Zhang, J. Wang, Y. Lan, H. Deng, J. Shen, R. Hu, Highly efficient bacteria-infected diabetic wound healing employing a melanin-reinforced biopolymer hydrogel, Chem. Eng. J. 460 (2023) 141852.

[44] S. Baghdasarian, B. Saleh, A. Baidya, H. Kim, M. Ghovvati, E.S. Sani, R. Haghniaz, S. Madhu, M. Kanelli, I. Noshadi, N. Annabi, Engineering a naturally derived hemostatic sealant for sealing internal organs, Mater. Today Bio 13 (2022) 100199.

[45] K.Y. Choi, O. Ajiteru, H. Hong, Y.J. Suh, M.T. Sultan, H. Lee, J.S. Lee, Y.J. Lee, O. J. Lee, S.H. Kim, C.H. Park, A digital light processing 3D-printed artificial skin model and full-thickness wound models using silk fibroin bioink, Acta Biomater. 164 (2023) 159–174.

[46] A. Baidya, M. Ghovvati, C. Lu, H. Naghsh-Nilchi, N. Annabi, Designing a nitro-induced sutured biomacromolecule to engineer electroconductive adhesive hydrogels, ACS Appl. Mater. Interfaces 14 (2022) 49483–49494.

[47] F.Z. Amourizi, A.Z. Malek-Khatabi, R. Zare-Dorabei, Polymeric and composite-based microneedles in drug delivery: regenerative medicine, microbial infection therapy, and cancer treatment, Mater. Chem. Horiz. 2 (2) (2023) 113–124.

[48] X. Qi, E. Cai, Y. Xiang, C. Zhang, X. Ge, J. Wang, Y. Lan, H. Xu, R. Hu, J. Shen, An immunomodulatory hydrogel by hyperthermia-assisted self-cascade glucose depletion and ROS scavenging for diabetic foot ulcer wound therapeutics, Adv. Mater. 35 (48) (2023) 2306632.

[49] H. Byun, Y. Han, E. Kim, I. Jun, J. Lee, H. Jeong, S.J. Huh, J. Joo, S.R. Shin, H. Shin, Cell-homing and immunomodulatory composite hydrogels for effective wound healing with neovascularization, Bioact. Mater. 36 (2024) 185–202.

[50] B. Kong, R. Liu, Y. Cheng, X. Cai, J. Liu, D. Zhang, H. Tan, Y. Zhao, Natural biopolymers derived hydrogels with injectable, self-healing, and tissue adhesive abilities for wound healing, Nano Res. 16 (2) (2022) 2798–2807.

[51] J. Guo, W. Sun, J.P. Kim, X. Lu, Q. Li, M. Lin, O. Mrowczynski, E.B. Rizk, J. Cheng, G. Qian, J. Yang, Development of tannin-inspired antimicrobial bioadhesives, Acta Biomater. 72 (2018) 35–44.

[52] K. Wu, M. Fu, Y. Zhao, E. Gerhard, Y. Li, J. Yang, J. Guo, Anti-oxidant anti-inflammatory and antibacterial tannin-crosslinked citrate-based mussel-inspired bioadhesives facilitate scarless wound healing, Bioact. Mater. 20 (2023) 93–110.

[53] C. Wang, Y. Luo, X. Liu, Z. Cui, Y. Zheng, Y. Liang, Z. Li, S. Zhu, J. Lei, X. Feng, S. Wu, The enhanced photocatalytic sterilization of MOF-Based nanohybrid for rapid and portable therapy of bacteria-infected open wounds, Bioact. Mater. 13 (2022) 200–211.

[54] S. Cheng, H. Wang, X. Pan, C. Zhang, K. Zhang, Z. Chen, W. Dong, A. Xie, X. Qi, Dendritic hydrogels with robust inherent antibacterial properties for promoting bacteria-infected wound healing, ACS Appl. Mater. Interfaces 14 (9) (2022) 11144–11155.

[55] J. Hwang, K.L. Kiick, M.O. Sullivan, Modified hyaluronic acid-collagen matrices trigger efficient gene transfer and prohealing behavior in fibroblasts for improved wound repair, Acta Biomater. 150 (2022) 138–153.